

東京大学 大学院新領域創成科学研究科
基盤科学研究系
先端エネルギー工学専攻

平成 21 年度

修士論文

A New Theory of a Microwave Supported Detonation

— マイクロ波支持デトネーションの新理論 —

2010 年 2 月提出
指導教員 小紫 公也 教授

66200 嶋田 豊

Contents

1. Introduction	3
1.1 Current status of launch vehicles	3
1.2 Laser Propulsion	5
1.3 Laser Thermal Exchange Thruster	7
1.4 Microwave Propulsion	7
1.4.1 Researches of Microwave Propulsion.....	7
1.4.2 Beam Transmission of Microwave Beam.....	7
1.5 Launch Cost Estimation of BEP	8
1.6 Detonation.....	9
2. Numerical Analysis of the Microwave Rocket.....	15
2.1 Numerical model.....	15
2.2 Microwave heating.....	18
2.3 Governing equations	21
2.4 Numerical method.....	21
2.4.1 Flux Difference Splitting [40].....	22
2.4.2 Flux Vector Splitting [40].....	23
2.4.3 SHUS (Simple High-resolution Upwind Scheme) [41].....	24
2.5 Grid resolution	25
2.6 Validation.....	26
2.7 Results.....	28
2.7.1 Microwave Supported Combustion (MSC) regime	29
2.7.2 C-J (Chapman-Jouget) MSC regime.....	31
2.7.3 Overdriven MSD (Microwave Supported Detonation) regime	33

2.7.4	Chapman-Jougen (CJ) MSD point.....	35
2.8	Flight performance.....	36
2.8.1	Momentum coupling coefficient.....	36
2.8.2	Thermal conversion efficiency	37
2.9	Theoretical discussion.....	38
2.9.1	MSC regime	41
2.9.2	C-J MSC regime	43
2.9.3	Overdriven MSD regime.....	44
2.9.4	C-J MSD point	45
2.10	Boundary between the MSC and MSD regime.....	47
2.11	A new theory for the Microwave Supported Detonation.....	49
3.	Chemical equilibrium calculation.....	57
3.1	Governing equations	57
3.2	Thermodynamic properties	59
3.3	Chemical equilibrium calculation	61
3.4	Verification	63
3.5	Calculation of the LSD wave	64
3.6	Results and discussions.....	66
4.	Conclusions	71

1. Introduction

1.1 Current status of launch vehicles

A great number of attracting space-exploration plans such as the space factory [1], Solar Power Satellite (SPS) [2], and homeostasis lunar base [3], have been proposed until today. However, most of these plans were abandoned mainly due to the high launch cost. Expendable Launch Vehicles (ELV) requires many heavy systems to launch a payload whose weight launched to Low Earth Orbit (LEO) is less than 4 % of the initial weight of the vehicle.[4] As a result, the current launch cost is as high as 5,000 \$/kg.[5]

Reusable Launch Vehicle (RLV) is a solution for cost reduction. However, as it has been clarified by Space Shuttle, RLV is a more complex system than ELV, and the cost reduction of RLV requires drastic technical breakthroughs: thermal protection systems for reentry and landing gears. At the same time, its structural weight must be as light as ELV.

The mass driver, in which a projectile is accelerated by a ground facility, is another solution for launch cost reduction. The projectile is a simple cargo to be launched, and even though a large investing is necessary for the infrastructures, the cost per launch can be reduced drastically. Ram accelerators [6][7] and Rail guns[8][9] are mass drivers candidates to launch an unmanned cargo at a high acceleration rate in the order of 10^4 m/s². A Ram accelerator is driven by chemical reactions of fuels filled in a long tube. In a Rail gun, a projectile is accelerated by the Lorentz force. These mass drivers are on the developing status, and achievable performance is uncertain at the present time. However in practical use, it may not be reasonable to accelerate a projectile to a hyper-sonic velocity on the ground because the projectile will suffer extremely severe

aerodynamic heating and loading. Thus these mass drivers will make the most sense in the space use.

Beamed energy propulsion (BEP) is a candidate for a low-cost launching, and can be considered as a mass driver. BEP is the system which gains propulsive energy by a high-power beamed electromagnetic wave transmitted from the ground or a space-based facility. Since BEP vehicles do not need to load an energy source such as a fuel tank, pumping system, electric source, or atomic reactors, the structure of a BEP propulsion thruster is very simple. Additionally, since the surrounding air can be used as a propellant during the flight in the atmosphere, the amount of propellant can be reduced and thus can achieve a high payload ratio.

In BEP, once the energy beam stations are built, it can be used for many launch counts. The constructing cost for such facilities will be predominant for few launch counts. Since the launch of a BEP vehicle itself costs lower than conventional rockets, the cost per launch can be reduced with the number of launch counts. The development cost for microwave oscillators is expected two orders of magnitude lower than that of laser, because a GW-class oscillator would be achievable by clustering existing high-power oscillators using the phased array technology. Then, microwave beaming propulsion is expected to achieve lower launch cost with fewer launch counts than laser beaming propulsion.

In open technical literatures, Kantrowitz first proposed a concept of a launching object using laser power supplied from a ground-based device in 1972.[10] Since then, beamed energy propulsion has intensively been nominated as a promising method of transporting vehicles with extreme low cost.

1.2 Laser Propulsion

From 70's through 80's, many studies were performed for 'flat-plate' type.[11][12][13][14] Intense laser beam was irradiated on a metallic plate surface in the atmospheric air to produce a high-pressure region on the surface as illustrated in Figure 1-1.[15]

Pirri et al. first studied laser pulsejet with a bell nozzle illustrated in Figure 1-2. The laser beam was focused by a parabola mirror to produce plasma. Expansion of the plasma drives a spherical blast wave in the surrounding air, and impulsive thrust is generated on the nozzle wall while a blast wave expands in the nozzle. Ageev et al. also studied the laser pulsejet experimentally using a parabola and a conical nozzle with a 5-J-pulse CO₂ laser.[16] In DLR (German Aerospace Center), a 53-g-Bell nozzle was launched to 60 cm high using a repetitive pulse laser whose average power was 7.9 kW (laser pulse energy was 175 J/pulse and repetition frequency was 45 Hz).[17]

In 1998, Myrabo et al. published the results of their flight demonstrations using a 10-kW-class repetitive pulse CO₂ laser.[18] Their demonstrations were world first, and recent researches on laser propulsion were activated by their report. A 'Lightcraft' used in the demonstrations is illustrated in Figure 1-1. An impulsive thrust is imparted on a spike nozzle, which focuses laser beam onto a cowl to produce plasma. Its mechanisms of impulse generation are same with those in the laser pulsejet though the geometry of focusing optics is different from the Bell type nozzle. One remarkable feature of the Lightcraft design is a front intake from which the air is taken and compressed.

A Laser In-Tube Accelerator (LITA)[19] is another variety of laser propulsion. LITA is a laser-driven ram accelerator where a projectile is accelerated by successive laser-induced explosions in a tube filled with a rare gas. Its thrust generation mechanisms are also quite similar to those of the laser pulsejet.

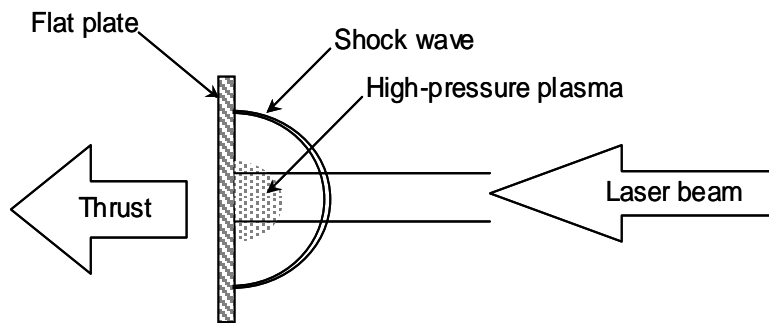


Figure 1-1 Flat plate type laser propulsion

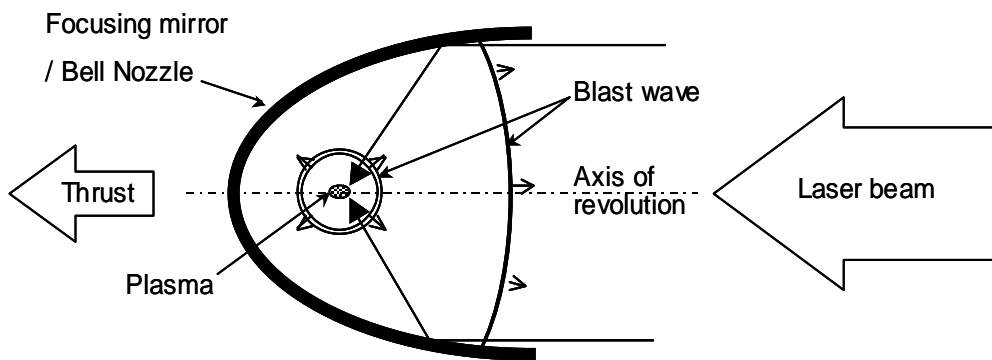


Figure 1-2 Laser pulsejet with a Bell nozzle

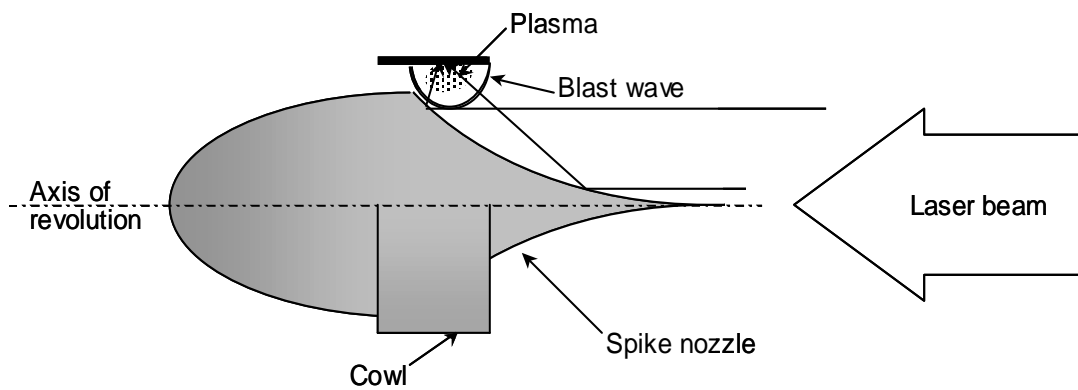


Figure 1-3 Lightcraft designed by Myrabo ¹⁸⁾

1.3 Laser Thermal Exchange Thruster

The concept of the thermal exchange rocket was proposed and studied by Kare. Instead of using plasma for the conversion of laser energy to thrust force, propellant is heated up to about 2700K and is exhausted using an aerodynamic nozzle. The design concept has similarity to the thermal atomic rocket and high specific impulse ($I_{sp}=500-700s$) was expected when hydrogen is applied for propellant.[20]

1.4 Microwave Propulsion

1.4.1 Researches of Microwave Propulsion

In the 1980s, Knecht conducted an analysis on microwave rocket system. In the thruster, propellant is heated by microwave in a dielectric chamber and is exhausted by a nozzle similar to a chemical rocket. Its specific impulse was estimated 2000s using hydrogen propellant.[21][22] Batanov also conducted analysis on a microwave rocket using $\lambda = 10mm$ microwave. The rocket nozzle was made from dielectric material to provide microwave power into the rocket. Thrust performance was estimated 50 W/kg.[23] Parkin et al. proposed a microwave thermal rocket. In their concept, a high power microwave heats a propellant in the dielectric heat exchanger tube and the heated propellant is exhausted using a nozzle similar to conventional rockets. Similar to laser thermal exchange rockets, propellant is heated up to about 2800K and exhausted from a nozzle.[24][25] They measured temperature of helium in a mullite tube using 2.45GHz microwave.[26]

1.4.2 Beam Transmission of Microwave Beam

In order to apply for the BEP launch system, microwave has to propagate long distance to provide energy to the vehicle. As an electromagnetic beam propagates long distances, the beam spot diverges. The radius of the diverged spot, due to the long

propagating distance of the electromagnetic beam, is obtained from a simple equation for a 0th Gaussian mode. Application of microwave to beamed energy propulsion is limited in frequencies in which the atmosphere is transparent. The advent of submillimeter astronomy has highlighted the existence of locations with particularly low atmospheric water content, opening up new microwave transmission windows between 35-300GHz and sometimes beyond. Since the atmospheric height of water vapor is only in the scale of 1-2km, sites such as the Caltech Submillimeter Observatory (CSO) on Mauna Kea are at high altitude, where atmospheric water vapor levels permit transmission above 250GHz, shown in Figure 1-4.

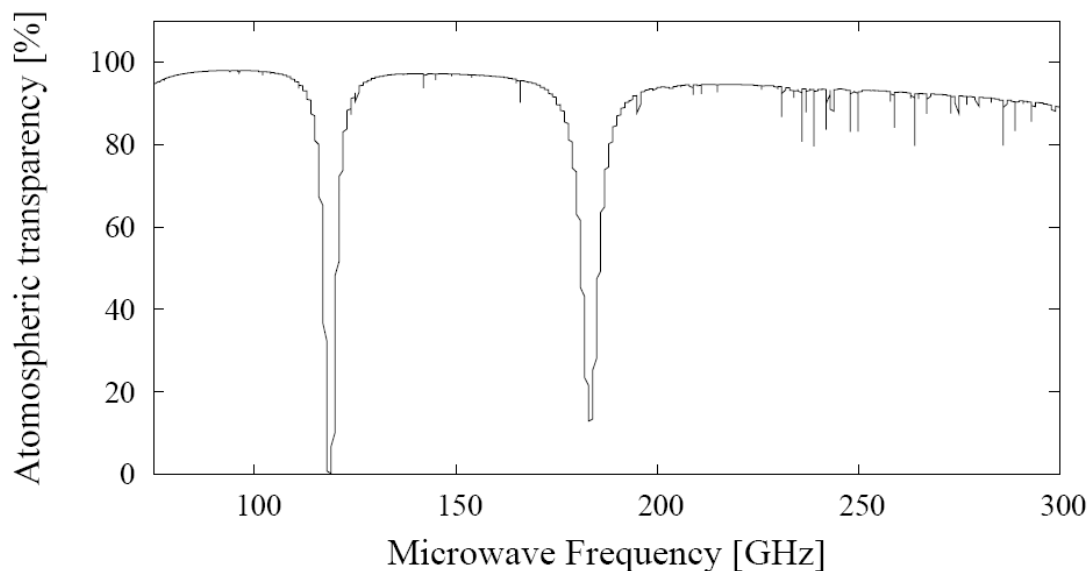


Figure 1-4 Beam transparency at millimeter wave band[27]

1.5 Launch Cost Estimation of BEP

Katsurayama et al. analytically examined feasibility of SSTO system powered by Repetitive Pulse laser and microwave. They proposed a vertical launch to minimize the development cost of the laser base. The vehicle is boosted by beamed energy propulsion to reach the orbit beyond the GEO. At the apogee point, the vehicle is kicked to GTO by an on-board motor, and decelerates at the perigee point in the similar way. This research

was focused on the construction of a 100-ton space solar power satellite in GEO. If a 1GW- output microwave facility becomes available, a vehicle could launch payload of 100kg. Along to their consideration, 1,000 launches are necessary, and cost becomes almost one-tenth of a chemical rockets' cost.[27][28][29] From these previous studies on the concepts and feasibilities, the application of the millimeter wave beam to BEP is expected as a promising technology.

1.6 Detonation

In the field of combustion dynamics, a flame propagating at a subsonic velocity is a phenomenon observed in usual life. This subsonic propagation of a flame is called a deflagration. On the other hand, a flame propagating supersonically is observed in extreme conditions; some applied in rocket engines, and some observed in explosion accidents. This phenomenon is called a detonation, which accompanies a shock wave. The difference between a deflagration and a detonation is listed in Table 1-1.

Table 1-1 Comparison between detonation and deflagration [30]

	Detonation	Deflagration
M_c	5~10	0.0001~0.03
u_2/u_1	0.4~0.7 (deceleration)	4~6 (acceleration)
p_2/p_1	13~55 (compression)	0.98 (slight expansion)
T_2/T_1	8~21 (heating)	4~16 (heating)
ρ_2/ρ_1	1.7~2.6	0.06~0.25

Experimental observations of detonation began about 130 years ago. At that time, explosion accidents, especially in mines, were major problems. In 1883, Mallard and Le Chatelier[31] published an article about experiments and theory of combustion and explosion, and pointed out that detonation was observed by Berthelot and Vieille.

Berthelot and Vieille[32] experimentally suggested that detonation is a combustion wave propagating at a specific velocity. At that time, research on shock waves has been highlighted and theoretical analysis on detonations was performed. This is when Hugoniot[33] and Chapman[34] made a theoretical discussion on detonation using the shock wave theory.

The theory of a steady one-dimensional detonation was made by Crussard[35] in 1907 and Jouget[36] in 1917. This is the widely known Chapman-Jouget (CJ) theory. By using hydrodynamic conservation equations, they pointed out that the detonation wave propagates at the minimum possible velocity. They concluded a simple theory saying that the propagating velocity could be determined only by the gas mixture, and not influenced by the chemical reaction rate.

In 1940, the structure of a detonation wave started to be discussed. A model explaining the structure using hydrodynamics, called the “ZND theory,” was proposed independently by three researchers: Zel’dovich in USSR[37], von Neumann in USA[38], Doering&Burkhardt in Germany[46].

The structure of a detonation wave explained in the ZND theory consists of a shock wave and a combustion region as shown in Figure 1-5. Here, a detonation wave propagating one-dimensionally in a quiescent premixed gas is schematically shown. The state in front the detonation wave, or the premixed gas, is shown by subscript 1 and state behind the detonation wave, or the burned gas, is shown by subscript 2. A shock wave propagating at a constant velocity u_1 compresses the premixed gas and increases the pressure and temperature to a state called the von Neumann spike. When the compressed gas reaches the explosion limit, ignition and chemical reaction occurs at a distance behind the shock wave. This distance between the shock wave and the reaction zone exists because of the time lag from the gas compression and ignition. By the

reaction taking place by the shock wave compression, detonation is observed as a supersonic combustion wave.

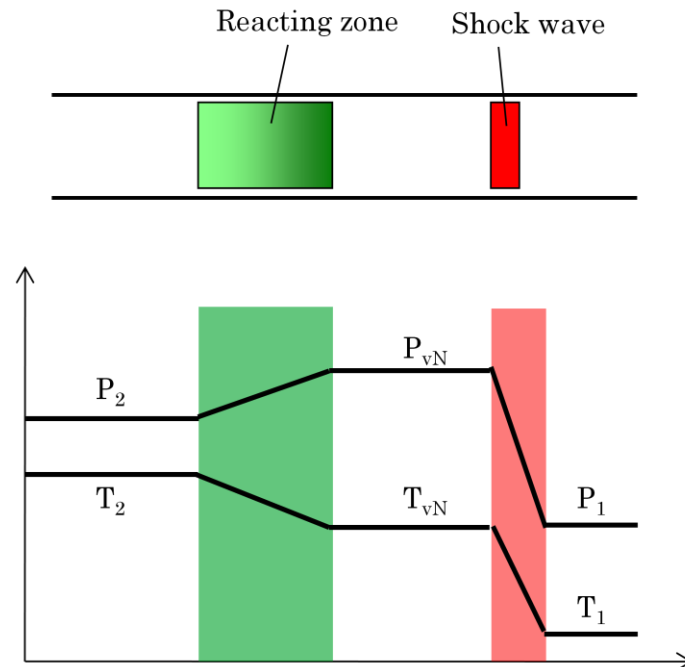


Figure 1-5 Structure of a detonation

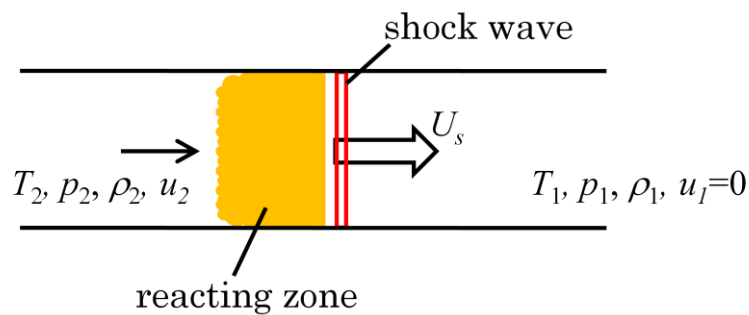


Figure 1-6 Propagating detonation in an observer fixed system of coordinates

In order to theoretically analyze we will consider a detonation propagating at a velocity of U_s , as in Figure 1-6. Then, a control volume around the detonation wave as shown in Figure 1-7. In order to set a control volume, a detonation fixed coordinate system is used here. Since the detonation wave is propagating at a constant velocity, the

state inside the control volume is steady. Here, the incoming flow is the premixed gas, and the outgoing flow is the burned gas.

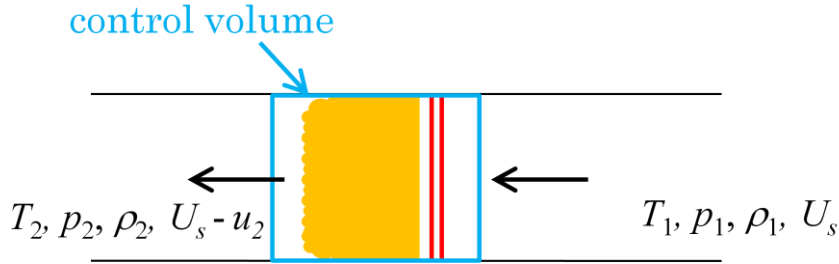


Figure 1-7 Propagating detonation in a detonation fixed system of coordinates

For simplicity, the inflow velocity U_s is changed to u_1 , and the outflow velocity $U_s - u_2$ is changed to u_2 . The governing equations for the flow field inside the control volume is the steady inviscid equations consisting of the conservation equations for mass, momentum and energy.

$$\rho_2 u_2 = \rho_1 u_1 \quad (1-1)$$

$$\rho_2 u_2^2 + p_2 = \rho_1 u_1^2 + p_1 \quad (1-2)$$

$$\frac{1}{2} u_2^2 + h_2 = \frac{1}{2} u_1^2 + h_1 + q \quad (1-3)$$

Here, ρ , u , p are density, velocity and pressure, respectively. In Eq. (1-3), h is the enthalpy. For a calorically perfect gas, the enthalpy is defined as $h = C_p T = \gamma R T / (\gamma - 1)$, and q is the heat production by the chemical reaction dependent only on the composition of the premixed gas. For simplicity, let us assume the entire gas as a calorically perfect gas, thus $\gamma = \text{const.}$ and $R = \text{const.}$

From Eqs. (1-1) and (1-2), the following relation is obtained:

$$\frac{p}{p_i} = \left(1 + \gamma M_i^2\right) - \gamma M_i^2 \frac{v}{v_i} \quad (1-4)$$

The above relation is called the Rayleigh line and the physical properties in a flow without friction changes along the Rayleigh line.

By substituting Eq. (1-3) into Eq. (1-4), the following relation is obtained:

$$\frac{p}{p_i} = \left(\frac{\gamma + 1}{\gamma - 1} - \frac{v}{v_i} + \frac{2q}{p_i v_i} \right) \bigg/ \left(\frac{\gamma + 1}{\gamma - 1} \frac{v}{v_i} - 1 \right) \quad (1-5)$$

The above relation is called the Hugoniot curve. Additionally, when the heat emission is $q=0$, the relation indicates the change at the shock wave, which is called the Shock adiabatic curve. The Rayleigh line, Hugoniot curve and the Shock adiabatic curve is shown in the p - v diagram in Figure 1-8. In a detonation described in the ZND model, a shock wave leads the reacting zone, thus the state discontinuously change along the Shock adiabatic curve from the state 1, in front of the shock wave, to state “vN.” vN stands for von Neumann, indicating the von Neumann spike. The pressure at state 2 corresponds to the von Neumann Spike. The state behind the shock wave changes continuously along the Rayleigh line. The contact point between the Rayleigh line and the Hugoniot curve is the Chapman-Jouget (C-J) point. For a Rayleigh line with a steeper slope, there exists two intersecting points with the Hugoniot curve. The upper intersecting point 2, indicates a strong detonation, in which the upstream is supersonic and the downstream is subsonic. This is called an Overdriven detonation, which propagates faster than the C-J velocity. Since the downstream is subsonic in an Overdriven detonation, the propagation is usually unstable. On the other hand, the lower intersecting point 2', indicates a weak detonation, in which the upstream and downstream is supersonic. Since the flow could only be accelerated to sonic speed in an exothermal reaction, a weak detonation is physically impossible. Thus state 2 is the only possible state behind the detonation wave. Especially, when the Rayleigh line is tangent to the

Hugoniot curve, the final state becomes the tangent point called the Chapman-Jouget (CJ) point. At this condition, the flow behind the detonation is at sonic speed.

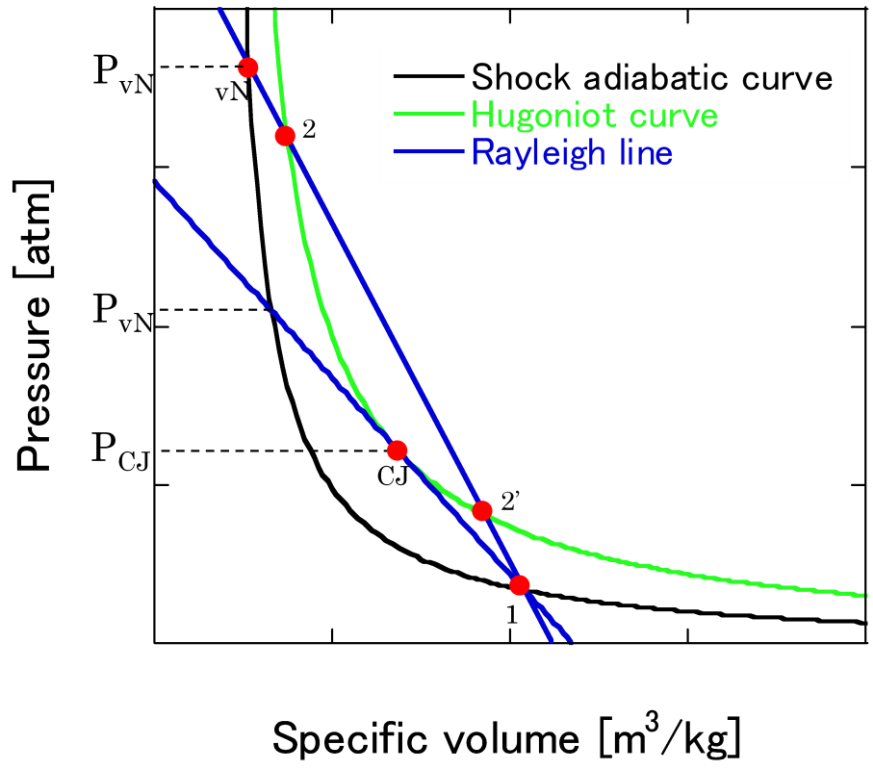


Figure 1-8 Hugoniot curve and Rayleigh line in a p-v diagram

2. Numerical Analysis of the Microwave Rocket

2.1 Numerical model

The plasma column formed in atmospheric air by a millimeter wave beam is shown in Figure 2-1. Figure 2-2 shows side-view photographs of the discharge development. As these figure shows, the ionization front propagates towards the upstream of the millimeter-wave beam at a constant velocity. Additionally, a heating region with a certain length is observed to propagate.

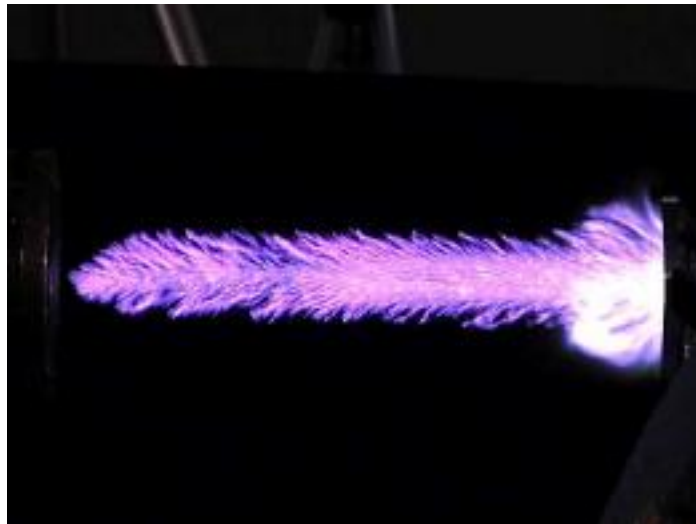


Figure 2-1 Photograph of Microwave Plasma, 700kW, $\tau=0.4\text{msec}$

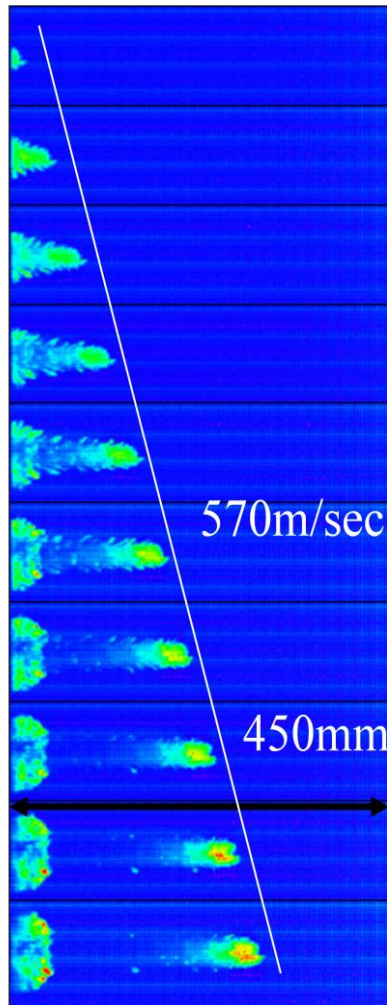


Figure 2-2 Photographic images of plasma propagation. P=730kW, 170GHz, $\tau=0.4\text{ms}$, 18,000FPS

As shown in Figure 2-3, measured propagation velocity of the ionization front, U_{ioniz} , increases with the peak power density S_0 . By linearly fitting the plotted results, we use the relations between U_{ioniz} [m/s] and S_0 [MW/cm^2] as follows:

$$U_{\text{ioniz}} = 4190S_0 - 14.9 \quad (2-1)$$

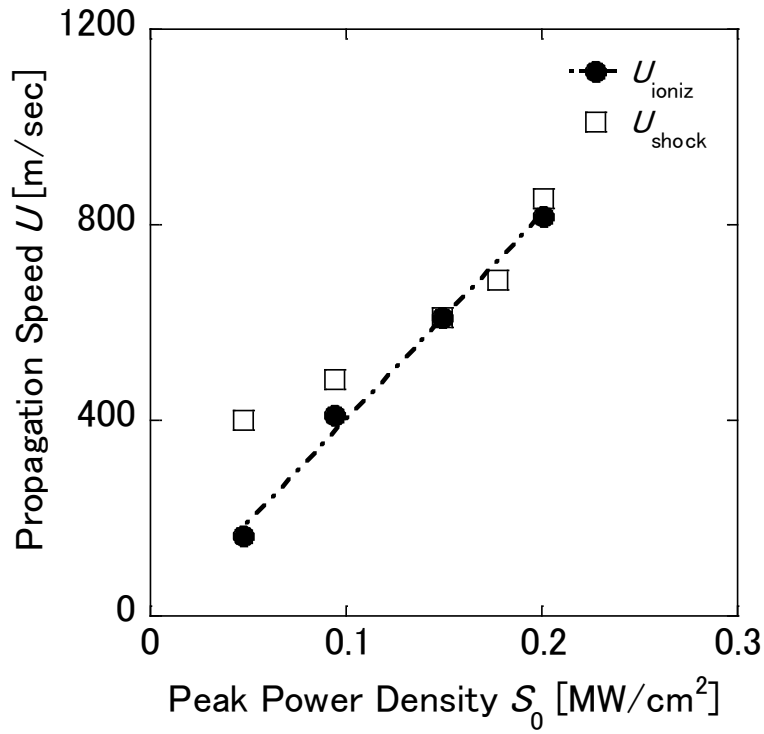


Figure 2-3 Dependence of U_{ioniz} and U_{shock} on S_0

A schematic figure of the Microwave Rocket is shown in Figure 2-4.

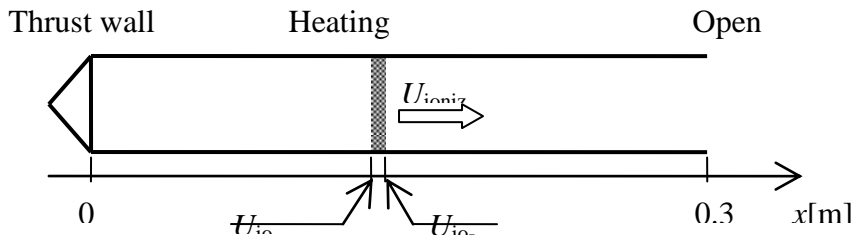


Figure 2-4 Calculation domain

The governing equations for the flow field are one-dimensional Euler equations, consisting of the conservation equations for mass, momentum and energy.

$$\frac{\partial \rho}{\partial t} + \frac{\partial \rho u}{\partial x} = 0 \quad (2-2)$$

$$\frac{\partial \rho u}{\partial t} + \frac{\partial}{\partial x} (\rho u^2 + p) = 0 \quad (2-3)$$

$$\frac{\partial E}{\partial t} + \frac{\partial}{\partial x}((E + p)u) = 0 \quad (2-4)$$

Here ρ is the density (mass per unit volume), ρu is the momentum per unit volume and E is the energy per unit volume. p is the pressure which is given as a function of the internal energy e and the density. For a perfect gas, the pressure has the form

$$p = \rho RT = (\gamma - 1)\rho e \quad (2-5)$$

$$e = \frac{E}{\rho} - \frac{1}{2}u^2 \quad (2-6)$$

where $\gamma = c_p/c_v$ is the ratio of specific heats, T is the temperature and R is the gas constant.

For a calorically perfect gas $e = c_v T$. Then

$$E = \rho e + \frac{1}{2}\rho u^2 = \rho c_v T + \frac{1}{2}\rho u^2 \quad (2-7)$$

2.2 Microwave heating

In the governing equations, the microwave energy should be added as a source term in order to simulate the microwave heating. In the atmospheric breakdown, ionized plasma absorbs the power of the microwave beam and air is heated. Since the ionization front propagates towards the beam source, the heating region also moves as the ionization front propagates.

On the millimeter wave beam, the electric field and the magnetic field are oscillating at the frequency of the millimeter wave. When the beam reaches the plasma, electrons in the plasma are accelerated by the oscillating electric field, thus obtaining kinetic energy from electromagnetic wave. The accelerated electrons collide with heavy particles and transfer the absorbed energy to other particles in the plasma. Therefore in the plasma heating region, air is heated by the radiation of the millimeter wave.

Various radiation models for air plasma are proposed, though we assume only ideal air which is heated by the microwave. Therefore, absorbed power density of the micro-

wave is given by $\eta S_{\text{average}}[\text{MW}/\text{cm}^2]$, and air is assumed to obtain energy. Here, S_{average} is the average microwave power density defined as follows:

$$S_{\text{average}} = \frac{P}{A} = \frac{2\omega_0^2}{d^2} S_0 \quad (2-8)$$

Here, P and A are the total output of the microwave and the cross section of the thruster, respectively. S_0 , ω_0 , d are the peak power density, beam waist, diameter of the plasma, respectively. The last relation is obtained from the relations of a Gaussian beam.

Since only part of the microwave energy is absorbed by the plasma, the energy absorption efficiency η , which is the ratio of the absorbed energy to the total beam energy, is defined. η is described as product of two parameters as follows:

$$\eta = \eta_{\text{coupling}} \times \eta_{\text{absorption}} \quad (2-9)$$

Here, the beam coupling efficiency η_{coupling} is defined as the ratio of the amount of power irradiated on the plasma to the total beam power. By observing the ionization front with a high-speed camera, luminescence of the plasma was observed in a radius shorter than the thruster, as illustrated in Figure 2-5. Since the microwave power is absorbed only by the plasma, the ratio of the absorbed component to the total output of microwave is necessary to take into consideration. This ratio could be calculated assuming axisymmetric plasma formed at the center of a Gaussian beam shown in Figure 2-5. Thus, η_{coupling} could be calculated as follows:

$$\eta_{\text{coupling}} = \frac{P(r_{\text{plasma}})}{P_{\text{beam}}} = \frac{P(\infty) \left[1 - \exp\left(-\frac{2r_{\text{plasma}}^2}{\omega^2}\right) \right]}{P_{\text{beam}}} \quad (2-10)$$

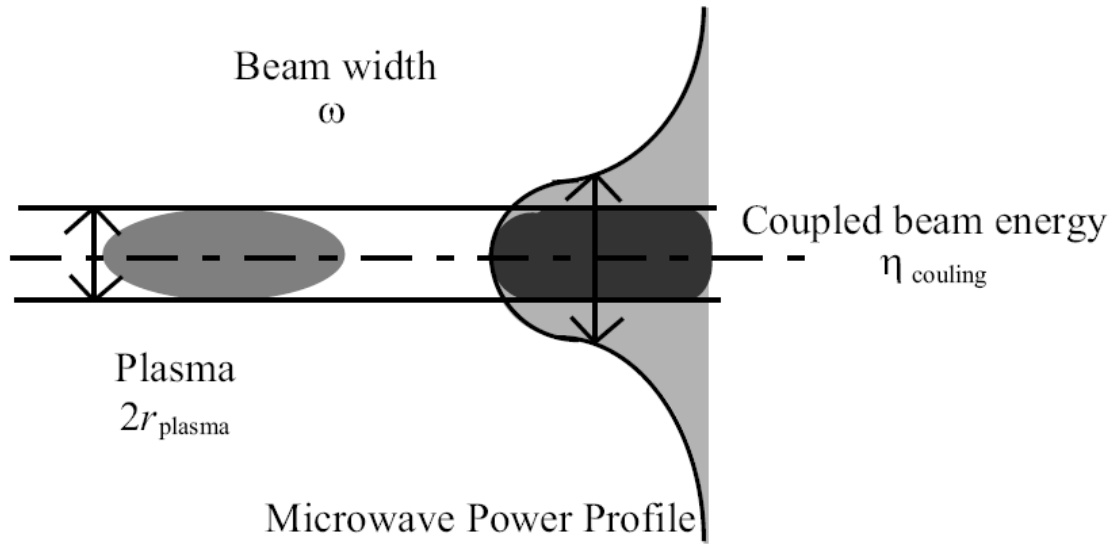


Figure 2-5 Schematic of the microwave beam profile and plasma

Here, r_{plasma} and ω are the radius of the plasma and the radius of the beam, respectively.

The absorption efficiency $\eta_{\text{absorption}}$ is defined as the ratio of the net microwave power absorbed by the plasma to the microwave power irradiated on the plasma. In the thermally equilibrium microwave plasma discussed in reference [7], some of microwave beam power is reflected from its surface due to the high electron density in the plasma. On the other hand, plasma supported by a CW laser cannot exceed the high electron number density which achieves the cut-off frequency for laser's wave length. Therefore some of laser beam power passes through the plasma. However, in the atmospheric millimeter wave plasma, both reflected and transparent power were not detected during the experiment. Therefore, $\eta_{\text{absorption}} = 1$ is assumed in this study.

Heating by the microwave is assumed to be uniform in a region with a length of λ : wavelength of the microwave. Therefore, the source term w in the energy equation of governing equations is as follows.

$$w = \frac{\eta S_{\text{average}}}{\lambda} \quad (\text{in a heating region}) \quad (2-11)$$

$$w = 0 \quad (\text{not in a heating region}) \quad (2-12)$$

2.3 Governing equations

$$\frac{\partial \mathbf{Q}}{\partial t} + \frac{\partial \mathbf{E}}{\partial x} = \mathbf{S} \quad (2-13)$$

$$\mathbf{Q} = \begin{bmatrix} \rho \\ \rho u \\ e \end{bmatrix}, \quad \mathbf{E} = \begin{bmatrix} \rho u \\ \rho u^2 + p \\ (e + p)u \end{bmatrix}, \quad \mathbf{S} = \begin{bmatrix} 0 \\ 0 \\ w \end{bmatrix} \quad (2-14)$$

2.4 Numerical method

The approximated Riemann problem is a typical initial-value problem which could be applied to any non-linear, parabolic system equations. By using the result obtained from the approximated Riemann problem, we could define the Godunov's method, which is a generalized upwind method for Euler equations. Defining the numerical flux at the cell interface as $E_{j+1/2}$, the Godunov's method for Eq. (2-13) is written as follows:

$$\frac{Q_j^{n+1} - Q_j^n}{\Delta t} + \frac{\Delta E^n}{\Delta x} = S \quad (2-15)$$

$$Q_j^{n+1} = Q_j^n - \frac{\Delta t}{\Delta x} [\tilde{E}_{j+1/2}^n - \tilde{E}_{j-1/2}^n] + \Delta t \cdot S \quad (2-16)$$

Since the Godunov's scheme itself only considers an approximated data, in which the physical values inside the cell is assumed constant, there is no need to obtain an exact solution for the Riemann problem. Thus, we only need to evaluate an approximated value for the numerical flux at the cell interface: $E_{j+1/2}$. There are mainly two methods to evaluate $E_{j+1/2}$; the Flux Difference Splitting (FDS) first proposed by Roe, and the Flux Vector Splitting (FVS) first proposed by Steger and Warming.

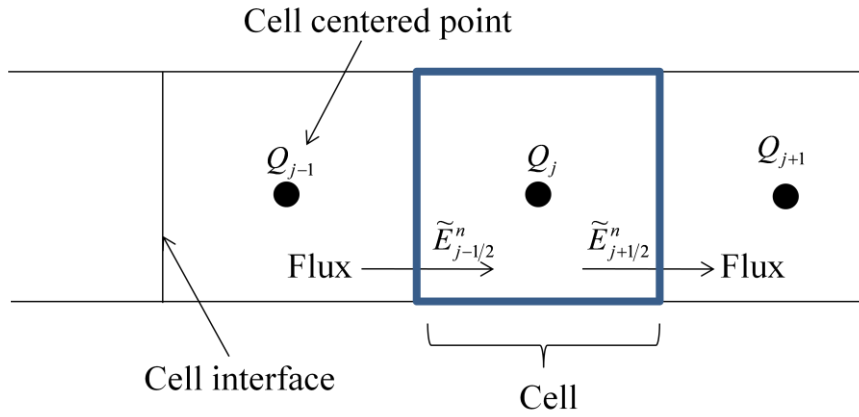


Figure 2-6 Computational cell in the Finite Volume Method

2.4.1 Flux Difference Splitting [40]

The numerical flux using FDS is defined as follows:

$$\tilde{E}_{j+1/2} = \frac{1}{2} [E_{j+1} + E_j - |A|_{j+1/2} (Q_{j+1} - Q_j)] \quad (2-17)$$

$$|A|_{j+1/2} = R_{j+1/2} |\Lambda|_{j+1/2} R_{j-1/2}^{-1} \quad (2-18)$$

Here, A , R and Λ are the flux Jacobian matrix, the characteristic matrix, and the diagonal matrix, respectively. For the Euler equations, the flux Jacobian matrix and the characteristic matrixes are written as follows:

$$A = \begin{bmatrix} 0 & 1 & 0 \\ -\frac{3-\gamma}{2}u^2 & (3-\gamma)u & \gamma-1 \\ \left(\frac{\gamma-1}{2}u^2 - H\right)u & H - (\gamma-1)u^2 & \gamma u \end{bmatrix} \quad (2-19)$$

$$R = \begin{bmatrix} 1 & 1 & 1 \\ u-c & u & u+c \\ H-uc & \frac{1}{2}u^2 & H+uc \end{bmatrix} \quad (2-20)$$

$$R^{-1} = \begin{bmatrix} \frac{1}{2} \left(b_1 + \frac{u}{c} \right) & -\frac{1}{2} \left(\frac{1}{c} + b_2 u \right) & \frac{1}{2} b_2 \\ 1 - b_1 & b_2 u & -b_2 \\ \frac{1}{2} \left(b_1 - \frac{u}{c} \right) & \frac{1}{2} \left(\frac{1}{c} - b_2 u \right) & \frac{1}{2} b_2 \end{bmatrix} \quad (2-21)$$

where,

$$H = \frac{e + p}{\rho} \quad (2-22)$$

$$b_1 = \frac{u^2}{2} \frac{\gamma - 1}{c^2}, \quad b_2 = \frac{\gamma - 1}{c^2}$$

2.4.2 Flux Vector Splitting [40]

The idea of FVS is to split the numerical flux, $E_{j+1/2}$, into two components: $E^+(Q)$ and $E^-(Q)$. Here, E^+ is the flux corresponding to the positive eigenvalues, and E^- corresponding to the negative eigenvalues. Since the information comes from the negative direction for the elements corresponding to the positive eigenvalues, a backward differential is applied. In the same way, a forward differential is applied for the elements corresponding to the negative eigenvalues. In order to split the flux, the diagonal matrix given from A^\mp is split as follows:

$$\Lambda^\pm = \frac{\Lambda \pm |\Lambda|}{2} \quad (2-23)$$

Here, Λ^+ consists only from the positive eigenvalues, and Λ^- consists only from the negative eigenvalues. Then, the following matrixes are defined:

$$A^\pm = R \Lambda^\pm R^{-1}, \quad E^\pm = A^\pm Q \quad (2-24)$$

By applying the split matrixes described above, the numerical flux using FVS is defined as follows:

$$\tilde{E}_{j+1/2} = E^+(Q_{j+1/2}) + E^-(Q_{j+1/2}) \quad (2-25)$$

2.4.3 SHUS (Simple High-resolution Upwind Scheme) [41]

As described above, FDS is a method directly applied from a scalar equation to a system equation. There are problems reported in simulating an impulsive start or inviscid expansion wave. A phenomenon called the carbuncle phenomenon also occurs easily in FDS. On the other hand, FVS is a method based on the idea of an advective flow. Some problems caused by FVS are the generation of a non-physical wiggle at the shock wave.

In order to solve these problems, Liou & Steffen proposed a method called AUSM, which splitted the advective term and pressure term similar to the FVS. Shima & Jounouchi further modified the method called a Uni-Particle Upwind Scheme, which handles the advective term as a single fluid particle. SHUS is one of the Uni-Particle Upwind Schemes which holds the following characteristics:

1. Enable to handle a boundary layer, or a steady/ unsteady contact surface
2. Not generating a severe carbuncle phenomena
3. Strong to shock waves or symmetric expansions

In order to describe the method, first the integrated form of the governing equations is written as follows:

$$\int \hat{\mathbf{Q}} dv + \int \hat{\mathbf{F}} ds = 0$$

$$\hat{\mathbf{F}} = m\mathbf{\Phi} + p\mathbf{N}, \quad \mathbf{\Phi} = \begin{bmatrix} 1 \\ u \\ H \end{bmatrix}, \quad \mathbf{N} = \begin{bmatrix} 0 \\ 1 \\ 0 \end{bmatrix}$$

$$m = \rho u$$

Here, $H = (e + p)/\rho$ is the total enthalpy. The flux is determined to choose the upwind side whether the mass flux m is positive or negative.

$$\tilde{\mathbf{P}} = \frac{m + |m|}{2} \dots_+ + \frac{m - |m|}{2} \dots_- + \tilde{p}\mathbf{N}$$

Subscript + indicates the left side of the cell, and – indicated the right side of the sell. By choosing how to evaluate the mass flux m , several schemes could be constructed. SHUS applies Roe’s FDS method, except uses primitive values instead of conservative values.

$$m = \frac{1}{2} \left\{ (\rho V_n)_+ + (\rho V_n)_- - |\bar{V}_n| \Delta \rho - \frac{|\bar{M} + 1| - |\bar{M} - 1|}{2} \bar{\rho} \Delta V_n - \frac{|\bar{M} + 1| + |\bar{M} - 1| - 2|\bar{M}|}{2} \frac{\Delta p}{\bar{c}} \right\}$$

$$M = \frac{\bar{V}_n}{\bar{c}}$$

Here, \bar{c} is the average of the sound velocity. The split pressure is given as follows:

$$\tilde{p} = \beta_+ p_+ + \beta_- p_-$$

where

$$\left\{ \begin{array}{ll} \beta_{\pm} = \frac{1}{4} (2 \pm M_{\mp}) (M_{\mp} \pm 1)^2 & |M_{\pm}| \leq 1 \\ \beta_+ = 1, \beta_- = 0 & M_{\pm} > 1 \\ \beta_+ = 0, \beta_- = 1 & M_{\pm} < 1 \end{array} \right.$$

2.5 Grid resolution

Grid convergence was evaluated by measuring τ_{plateau} : the time of pressure maintained for thrust. Here, τ_{plateau} is given by integrating the time of shock wave and expansion wave inside the thruster, thus it is important to understand the grid convergence. Calculated τ_{plateau} for each grid points is shown in Figure 2-7. The horizontal axis shows the grid number in the heating region, λ/dx . The evaluation was conducted under the condition of microwave power density at $S_0=0.120, 0.320 \text{ MW/cm}^2$. In both cases, the calculated result show that τ_{plateau} converged at a region of $\lambda/dx > 10$. At the present calculation, we set the cell length at $dx=5.0 \times 10^{-5} \text{ m}$, where the grid number at heating region is, $\lambda/dx \doteq 35$.

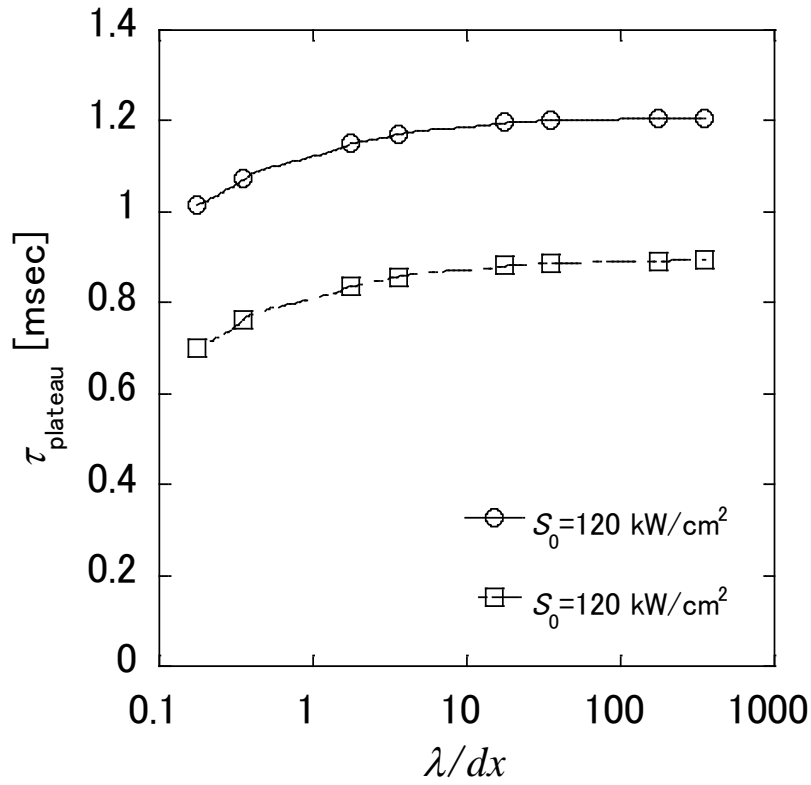


Figure 2-7 Grid convergence

2.6 Validation

Numerical results of U_{shock} and p_3 were compared with experimental results. Here, U_{shock} and p_3 are propagation velocity of shockwave and thrust pressure, respectively. Results for each microwave power are shown in Figure 2-8 for p_3 , and in Figure 2-9 for U_{shock} .

Both results showed good agreement with experimental results. Therefore, we obtained the detailed structure of internal flow field, and the structure of a microwave supported detonation will be discussed.

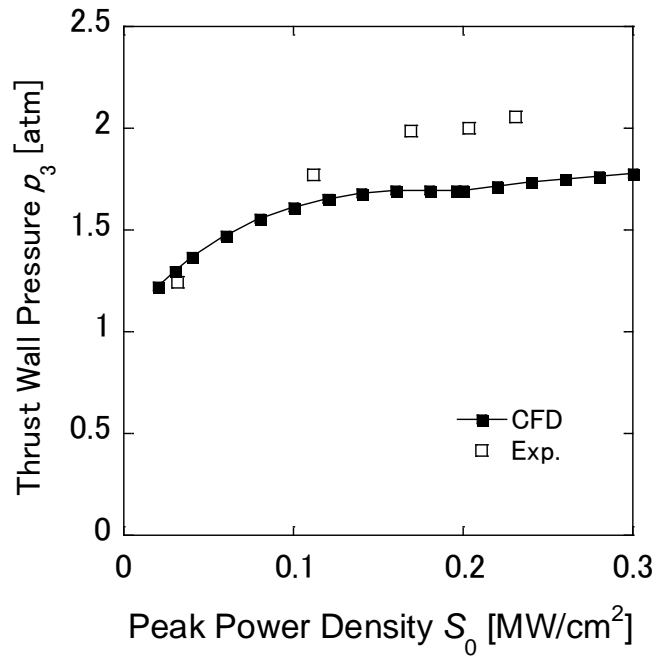


Figure 2-8 Comparison of thrust wall pressure

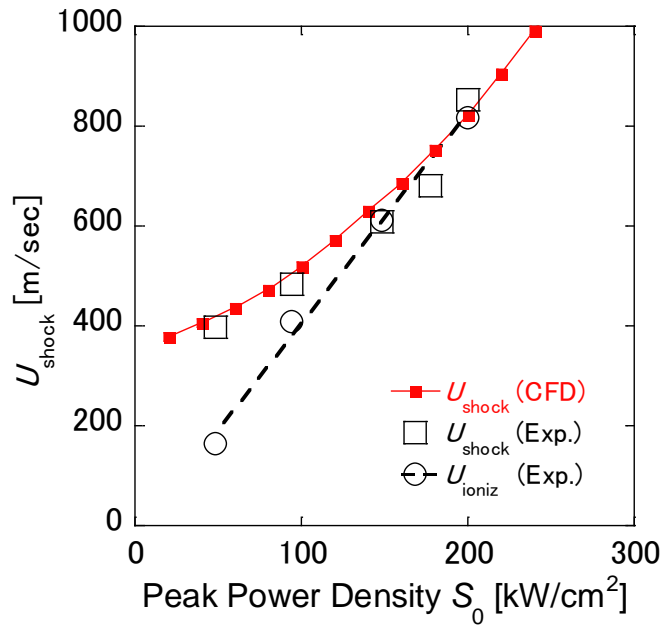


Figure 2-9 Comparison of propagating velocity of shock wave

2.7 Results

As shown in Figure 2-10, the flow field is categorized into three regimes and one point, namely the MSC regime, the C-J MSC regime, the Overdriven MSD regime and the C-J MSD point. The Microwave Supported Combustion (MSC) regime is when the microwave power density is lower than 0.121 MW/cm^2 . The Chapman-Jouget (C-J) MSC regime is in the range of power density of $0.121 < S_0 < 0.196 \text{ MW/cm}^2$. At the power density of $S_0 > 0.196 \text{ MW/cm}^2$, the propagating velocity of the shock wave and the ionization front becomes the same. Since a detonation is defined as a phenomenon where a reacting zone and a shock wave propagate together at a same velocity, here we define this region as the Microwave Supported Detonation (MSD) regime. Especially when $S_0 = 0.196 \text{ MW/cm}^2$, the propagating velocity is defined as the minimum possible velocity for the detonation, or the C-J velocity, here we call this point as the C-J MSD regime.

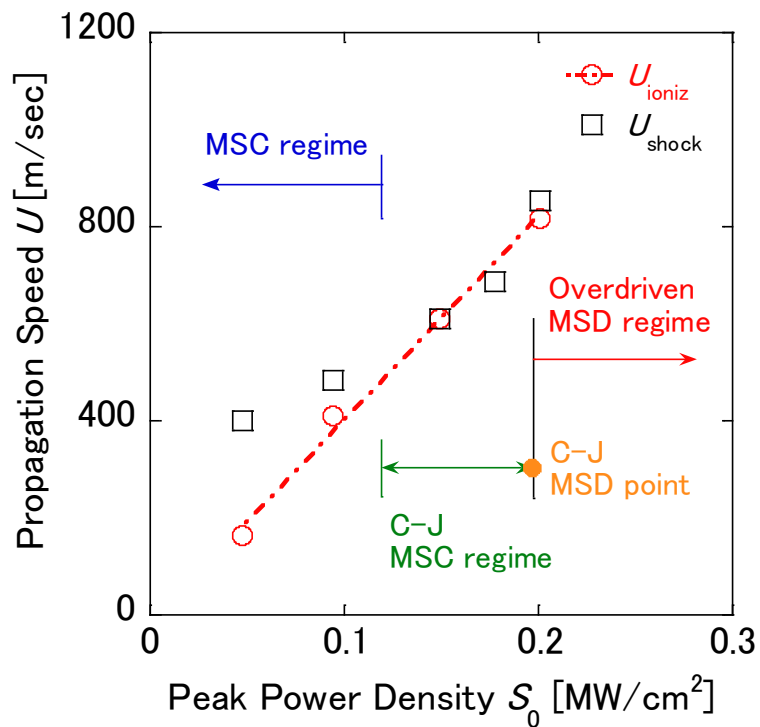


Figure 2-10 Definition of regimes in flow field

2.7.1 Microwave Supported Combustion (MSC) regime

An $x-t$ diagram is shown in Figure 2-11, whose horizontal axis is the position and the vertical axis is time. Here, two discontinuities propagating at a constant, but in a different, velocity could be seen. The discontinuity propagating in the lower velocity corresponds to the heating region, which was originally set to propagate at a constant velocity. The other discontinuity, propagating faster, corresponds to the shock wave. Thus in the MSC regime, it could be said that by setting the heating region to propagate at a constant velocity, the shock wave would be simulated to propagate at a constant velocity.

In order to further discuss into the flow field, temperature and pressure distributions are shown in Figure 2-12. The horizontal axis shows the position in the long direction where $x=0$ is the thrust wall and $x=0.3$ the exit. As seen in Figure 2-12, two disconti-

nuous steps propagate toward the exit. The left discontinuity is the heating region given by Eq. (2-1), and the right discontinuity is the shock wave propagating in front the heating region. Both discontinuities propagate at a constant velocity, thus the distance between increases with time. In order to analyze the flow field, we set three states: 1 as the state in front of the shock wave, 2 as the state between the shock wave and heating region, 3 as the state behind the heating region. Theoretical discussions are made later.

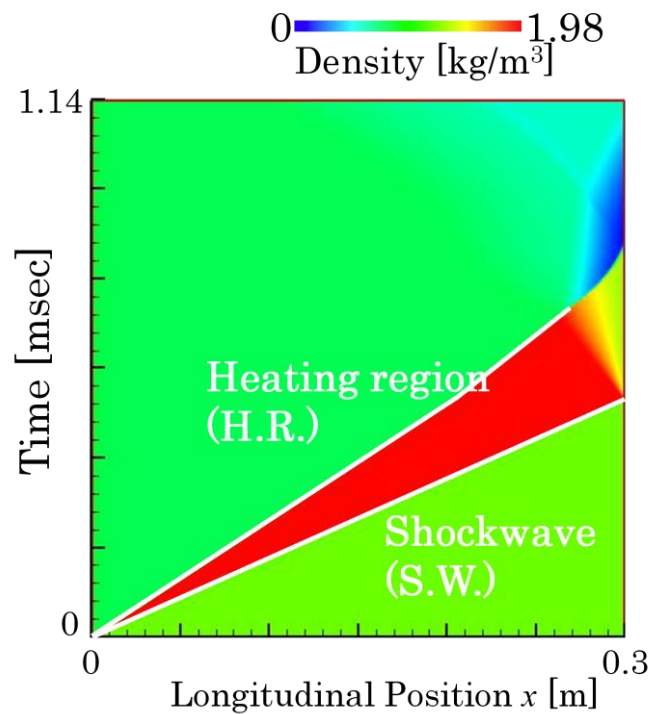


Figure 2-11 $x-t$ diagram in the MSC regime

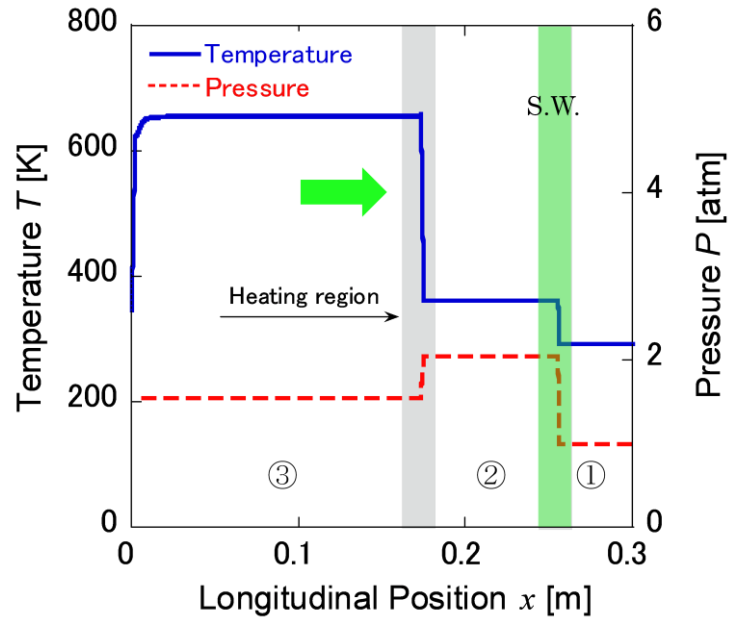


Figure 2-12 Longitudinal distribution of pressure and temperature in the MSC regime

2.7.2 C-J (Chapman-Jouget) MSC regime

By increasing the microwave power, the flow field changes to Chapman-Jouget(C-J) MSC regime. An $x-t$ diagram is shown in Figure 2-13. Although the two discontinuities are observed to propagate at a close velocity, there are still two discontinuities observed which is similar to the MSC regime.

Temperature and pressure distribution are shown in Figure 2-14. As it is shown in Figure 2-12, the horizontal axis shows the position in the long direction where $x=0$ is the thrust wall and $x=0.3$ the exit. In Figure 2-14, the left discontinuity is the heating region, and the right discontinuity is the shock wave. Although two discontinuities propagate toward the exit which is similar to the MSC regime, the difference is that a gradient is generated behind the heating region. In order to analyze the flow field, we set four states: 1 as the state in front of the shock wave, 2 as the state between the shock wave, 2.5 as the state between the heating region and the gradient, and 3 as the state behind the gradient.

The expansion wave behind the heating region shows different tendencies to MSC regime. Local Mach number at the head of the expansion wave were $M_3=1$ throughout this regime. Thus, the expansion wave was generated because the flow was thermally choked. This expansion wave was identified when the microwave power density was over $S_0=0.121 \text{ MW/cm}^2$.

C-J MSC regime is obtained when the microwave power density is at $0.121 \leq S_0 \leq 0.196 \text{ MW/cm}^2$. In this region, thermal choke occur. Since the velocity of each discontinuity is different, it still could not be called as a detonation. Additionally, since the local Mach number behind the heating region was $M=1$ throughout this regime, it could be said that the flow is in C-J state. Therefore, here we define this region as C-J MSC regime.

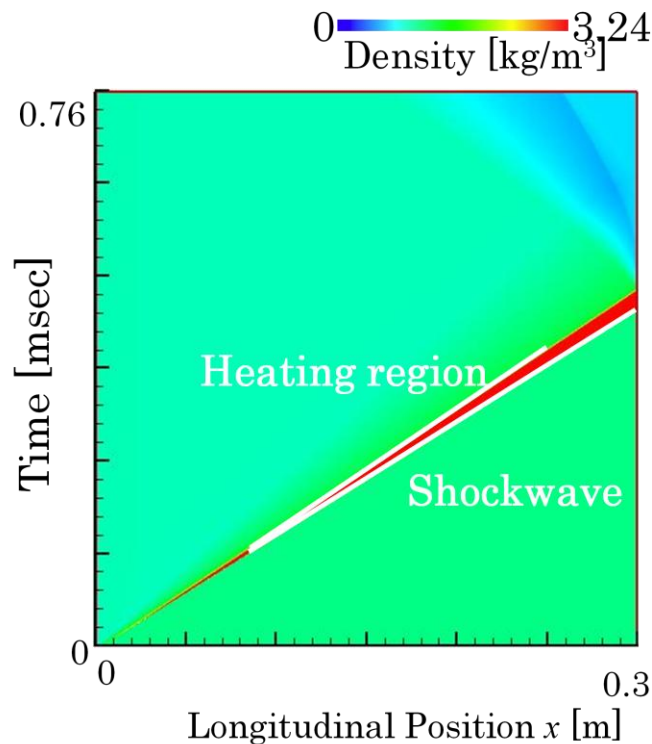


Figure 2-13 x-t diagram in the C-J MSC regime

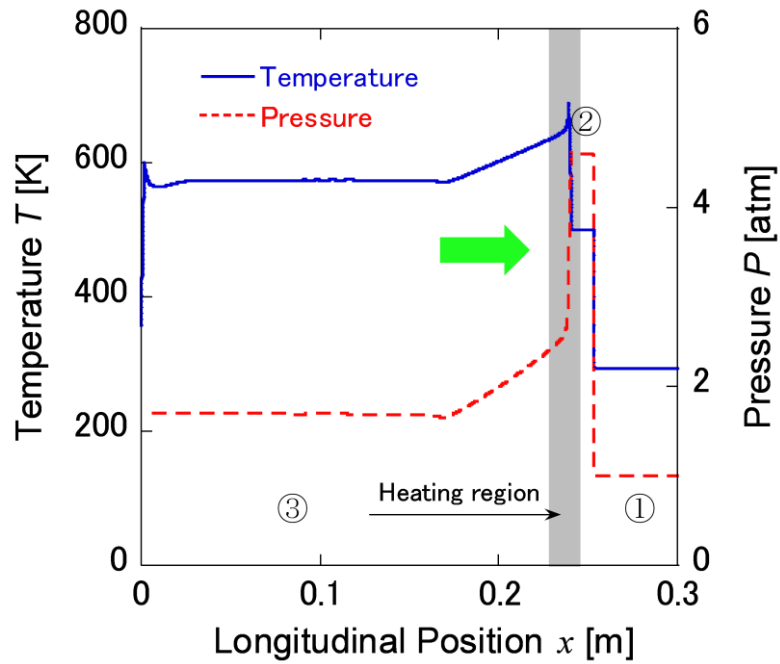


Figure 2-14 Longitudinal distribution of pressure and temperature in the C-J MSC regime

2.7.3 Overdriven MSD (Microwave Supported Detonation) regime

The regime with the highest microwave power densities are the Overdriven MSD regime. Temperature and pressure distributions are shown in Figure 2-16.

Here in the Overdriven MSD regime, both temperature and pressure has only one discontinuity. After a flat region, an expansion wave propagates. In order to analyze the flow field, we set three states: 1 as the state in front of the discontinuity, 2 as the state where the distribution is flat, and 3 as the state behind the gradient.

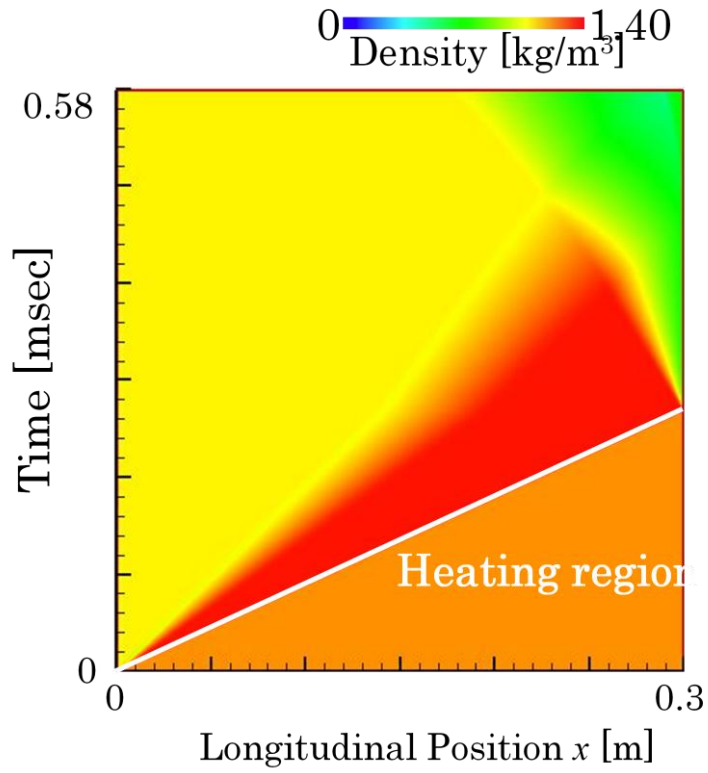


Figure 2-15 $x-t$ diagram in the Overdriven MSD regime

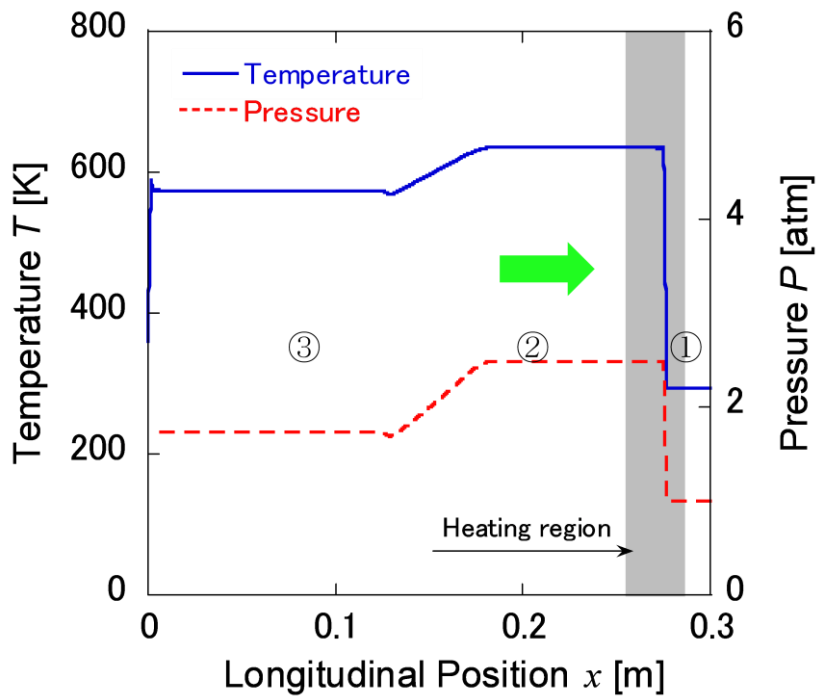


Figure 2-16 Longitudinal distribution of pressure and temperature in the Overdriven MSD regime

2.7.4 Chapman-Jougen (CJ) MSD point

When the microwave power is at $S_0=0.196 \text{ MW/cm}^2$, the velocity of heating region and shockwave become equal. Thus at this point, the propagating wave could be called a detonation. Additionally, since the flow is thermally choked, it is in C-J state. This specific point at $S_0=0.196 \text{ MW/cm}^2$ is called the C-J MSD point. This point says that when the velocity of the heating region and shock wave becomes equal, the two discontinuities attach and becomes a single discontinuity, as shown in Figure 2-17.

In the present phenomena and numerical model, heating region does not propagate by shockwave compression. Therefore, the structure differs from the ZND detonation model. Theoretical analysis on the wave structure will be discussed in the next chapter.

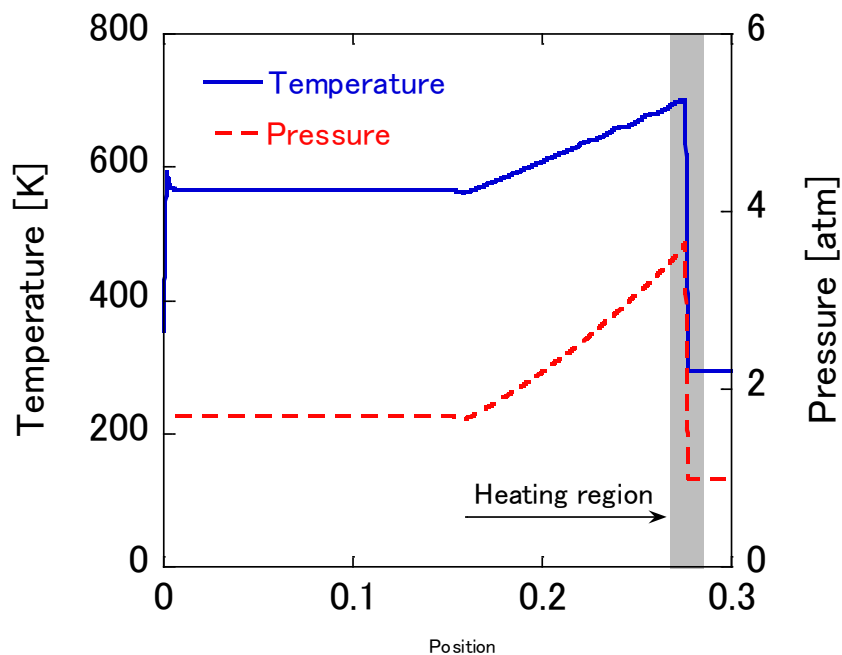


Figure 2-17 Longitudinal distribution of pressure and temperature in the C-J MSD point

2.8 Flight performance

2.8.1 Momentum coupling coefficient

In beamed energy propulsion, it is important to estimate the ratio of the input laser energy and thrust produced. Momentum coupling coefficient is commonly used to evaluate the performance for a beamed energy rocket. In the present research, momentum produced during a single cycle, and momentum coupling coefficient is estimated as follows:

$$I = A(p_3 - p_1)\tau_{plateau} \quad (2-26)$$

$$C_m = \frac{I}{P\tau_{pulse}} \quad (2-27)$$

Here, p_1 and p_3 are thrust pressure and atmospheric pressure, respectively. Additionally, $\tau_{plateau}$, and τ_{pulse} are the time of thrust pressure kept, and pulse duration, respectively. Calculated and experimentally measured momentum coupling coefficient for each microwave power density is shown in Figure 2-18.

Calculated results show that the distribution of C_m gradually decreases after a maximum value. This trend is similar to experimental results. The maximum value appears at the C-J MSC regime. This indicates that the maximum heat transfer to the flow field contributed to the increase in thrust performance.

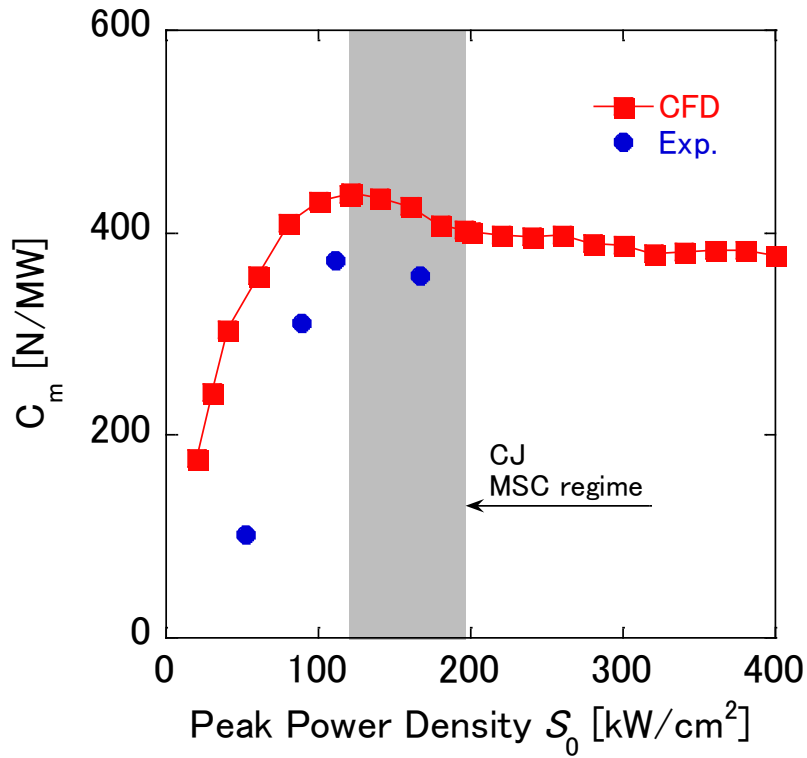


Figure 2-18 Calculated and measured C_m for each power densities

2.8.2 Thermal conversion efficiency

Thermal conversion efficiency was calculated based on the Pulse Detonation Engine (PDE) model [42][43]. Calculated results are shown in Figure 2-19. As it was with the distribution of C_m , distribution of thermal conversion efficiency shows a maximum value at C-J MSC regime. Here also indicates that the maximum heating in the C-J MSC regime produced maximum flow work.

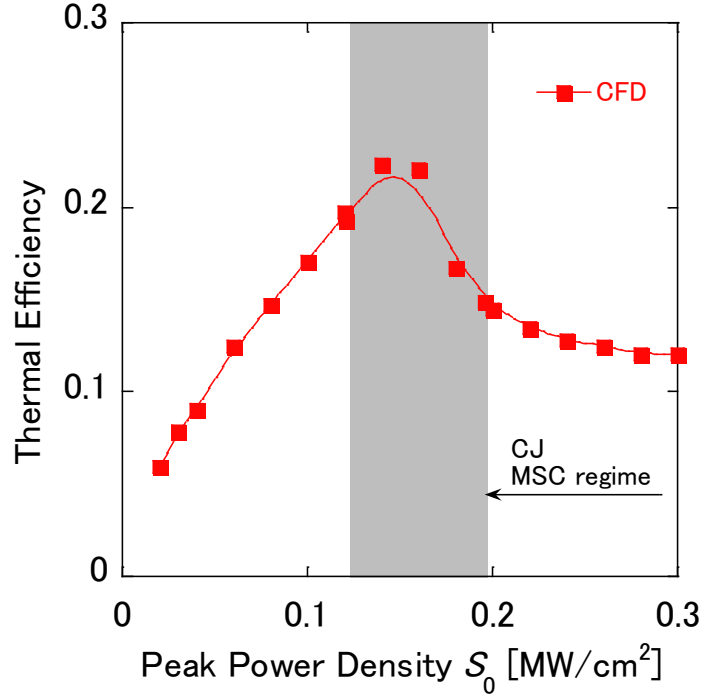


Figure 2-19 Calculated thermal efficiency for each power densities

Above all, we predict that the performance for a microwave rocket will be optimized at the C-J MSC regime, where the microwave power is $0.121 \leq S_0 \leq 0.196$ MW/cm².

2.9 Theoretical discussion

If we set a control volume around a flow field, we can apply the hydrodynamic equations as follows:

$$\frac{\partial}{\partial t} \int_{V_0} \rho dV = - \oint_{S_0} \rho \mathbf{u} \cdot \mathbf{n} dS \quad (2-28)$$

$$\frac{\partial}{\partial t} \int_{V_0} \rho \mathbf{u} dV = - \oint_{S_0} \{ p \mathbf{n} + \mathbf{u} (\rho \mathbf{u} \cdot \mathbf{n}) \} dS + \oint_{S_0} \boldsymbol{\sigma}' \cdot \mathbf{n} dS \quad (2-29)$$

$$\frac{\partial}{\partial t} \int_{V_0} \rho \left(\frac{1}{2} u^2 + e \right) dV = - \oint_{S_0} \left\{ \rho \mathbf{u} \left(\frac{1}{2} u^2 + h \right) - \mathbf{u} \cdot \boldsymbol{\sigma}' + q \right\} \cdot \mathbf{n} dS \quad (2-30)$$

Here, ρ , u , e , σ' , q are the density, velocity, energy per unit volume, viscous stress tensor and energy flux, respectively. Additionally, V_0 and S_0 are the volume and the surface area of the control volume.

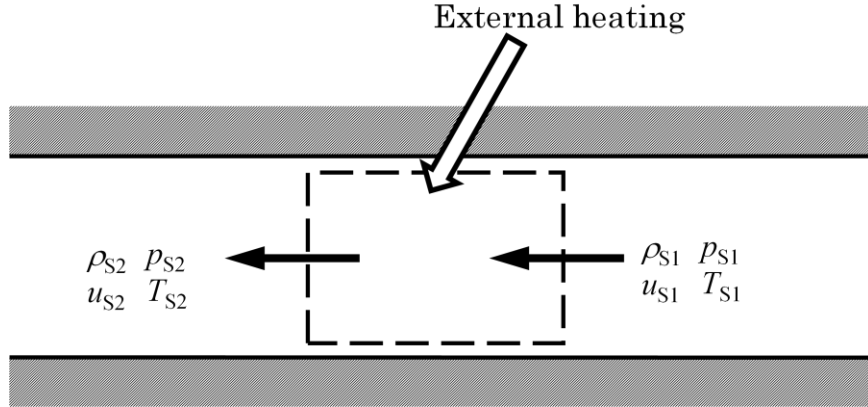


Figure 2-20 Control volume for the Rayleigh flow

If we assume a steady state in the control volume, the time derivative, or the left hand side, in Eqs. (2-28)-(2-30) will vanish. Furthermore, the equations could be simplified by assuming a one-dimensional flow as shown in Figure 2-20. Thus, the governing equations to be considered are written as follows:

$$\rho_i u_i = \rho u \quad (2-31)$$

$$p_i + \rho_i u_i^2 = p + \rho u^2 \quad (2-32)$$

$$C_p T_i + \frac{1}{2} u_i^2 + q = C_p T + \frac{1}{2} u^2 \quad (2-33)$$

Here, subscription i indicates the incoming flow, and the outgoing flow is shown with no subscription. For chemical detonations, q is the heat produced by combustion, or also defined as the change in formation enthalpy between the premixed gas and the burnt gas. In case of a beamed energy used, the heating ratio is given as $q = \eta S_0 / \rho_i u_i$. In the present model, an idealistic gas is assumed. Therefore the amount of heating is given only from the microwave. From Eqs. (2-31) and (2-32), the following relation is given.

$$\frac{P}{P_i} = (1 + \gamma M_i^2) - \gamma M_i^2 \frac{v}{v_i} \quad (2-34)$$

Here, M_i is the inflow Mach number, and v is the specific volume defined as $v=1/\rho$. The above relation is represented as a line on a pressure-specific volume diagram, or the p - v

Figure 2-21
diagram, as shown in

This line is determined by the physical state and the velocity of the inflow, and is called the Rayleigh line.

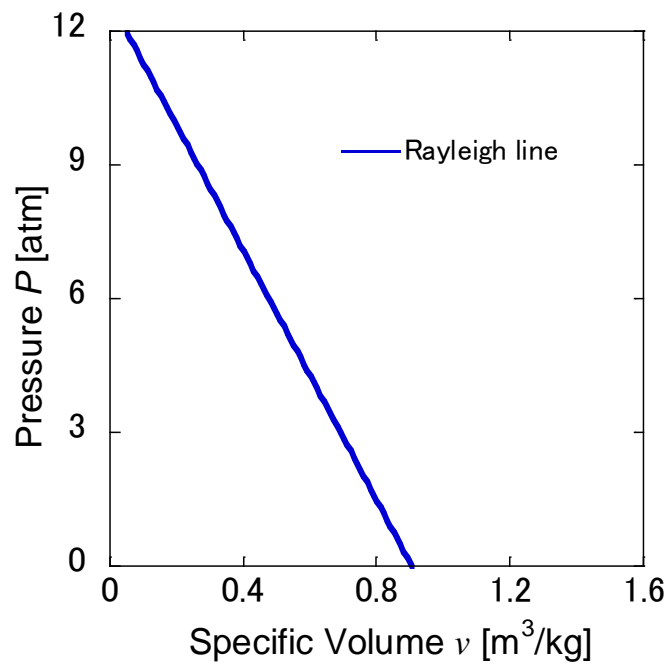


Figure 2-21 Rayleigh line in a p - v diagram

From Eqs. (2-31)-(2-33), the following relation is given.

$$\frac{p}{P_i} = \left(\frac{\gamma + 1}{\gamma - 1} - \frac{v}{v_i} + \frac{2q}{P_i v_i} \right) \left/ \left(\frac{\gamma + 1}{\gamma - 1} \frac{v}{v_i} - 1 \right) \right. \quad (2-35)$$

The above relation is represented as a curve on the p - v diagram, as shown in Figure 2-22. This curve is called the Hugoniot curve, and it shifts to the upper right as q increases. Especially when $q=0$, the relation represents a flow with no external heating, which becomes the shock wave relations. Thus, the curve in the p - v diagram when $q=0$ is called the Shock adiabatic curve, and represents the relations between the upstream and downstream of a shock wave.

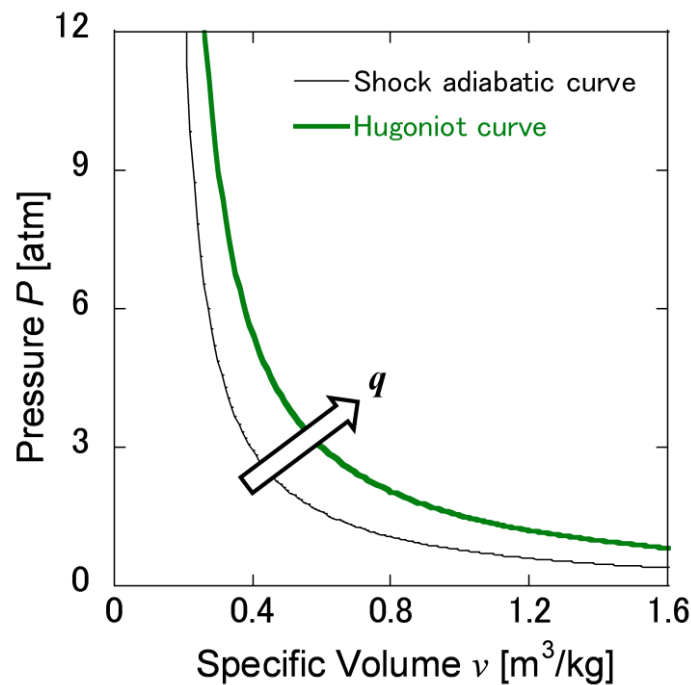


Figure 2-22 Hugoniot curve in a p - v diagram

2.9.1 MSC regime

In Figure 2-12, three states were determined in the flow field: 1 as the state in front of the shock wave, 2 as the state between the shock wave and heating region, 3 as the state behind the heating region. The p - v diagram for MSC regime is shown in Figure 2-24. Downstream of the heating region satisfies Eqs. (2-34) and (2-35), thus the change at the heating region is given by the intersection point of a Rayleigh line and Hugoniot

curve in the $p-v$ diagram. Additionally, when there is no heating, $q=0$, Eqs. (2-31)-(2-33) indicate a conservation law for a shock wave. Therefore, a curve given by Eq. (2-35) with $q=0$ is called the shock adiabatic curve. Furthermore, the downstream of a shock wave is given by an intersection point of a Rayleigh line and shock adiabatic curve.

In Figure 2-24, state 2 is given by an intersection point of the shock adiabatic curve and Rayleigh line 1 starting with state 1. Additionally, state 3 is given by an intersection point of the Rayleigh line 2 starting with state 2, and Hugoniot curve. Therefore, we understand that MSC regime consists of a shock wave and Rayleigh flow.

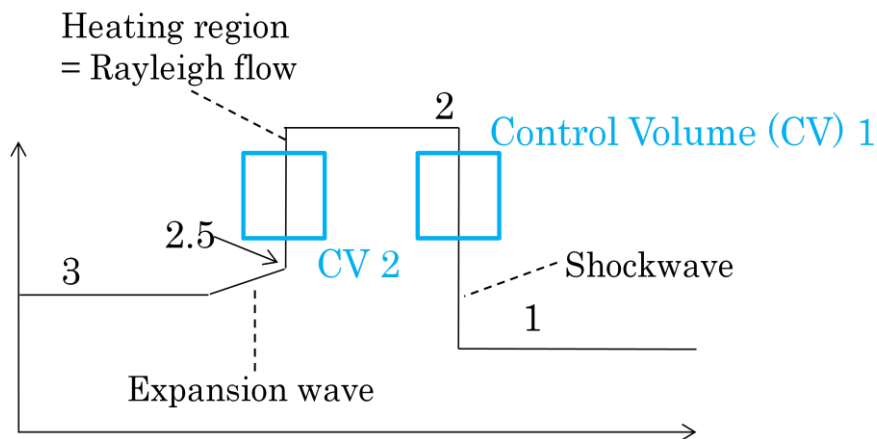


Figure 2-23 Control volumes for the MSC and C-J MSC regime

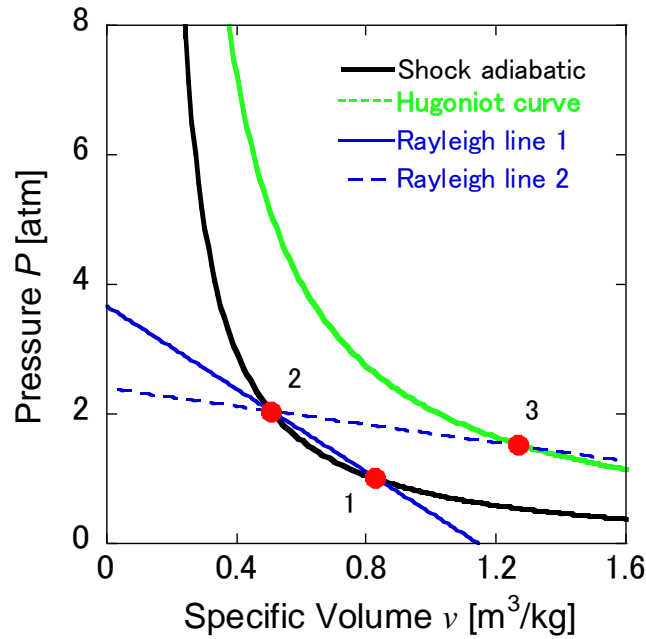


Figure 2-24 p - v diagram for the MSC regime

2.9.2 C-J MSC regime

In Figure 2-14, four states were determined: 1 as the state in front of the shock wave, 2 as the state between the shock wave, 2.5 as the state between the heating region and the gradient, and 3 as the state behind the gradient. The p - v diagram for C-J MSC regime is shown in Figure 2-25. State 2 is given by the intersecting point of Rayleigh line 1 starting with state 1, and shock adiabat curve. Similarly, state 2.5 is given by the intersecting point of Rayleigh line 2 starting with state 2 and Hugoniot curve. Here, Hugoniot curve shifts to the upper right in the p - v diagram as the heating q increases. On the other hand, the gradient of the Rayleigh line is determined by the inflow Mach number. Thus, the Rayleigh line tangent to the Hugoniot curve indicates that the heating to the flow field is at maximum amount. Therefore, thermal choke occur to the flow field in this condition at C-J MSD regime.

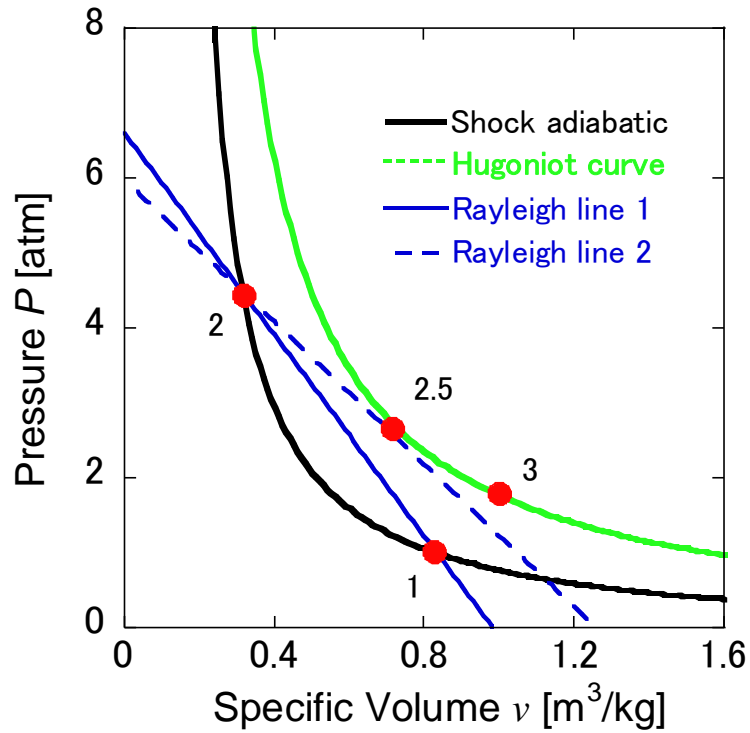


Figure 2-25 p - v diagram for the C-J MSC regime

2.9.3 Overdriven MSD regime

Temperature rise in Overdriven MSD regime occurs at the heating region, which indicates the use of the Rayleigh flow relations. A p - v diagram for Overdriven MSD regime is shown in Figure 2-27. State 2 is a intersecting point of the Rayleigh line and Hugoniot curve. This indicates that the change from state 1 to 2 is done by a heating process without a shockwave compression. Therefore, Overdriven MSD regime consists of a Rayleigh flow and an expansion wave.

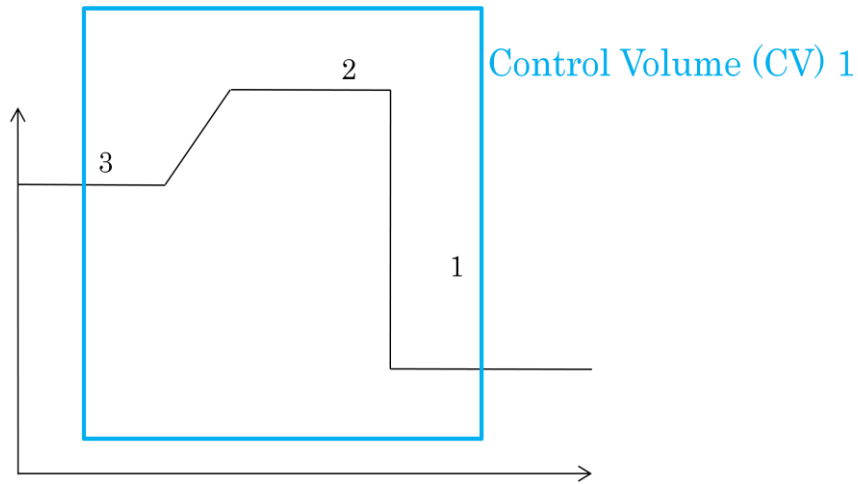


Figure 2-26 Control volume for the C-J MSD and Overdriven MSD regime

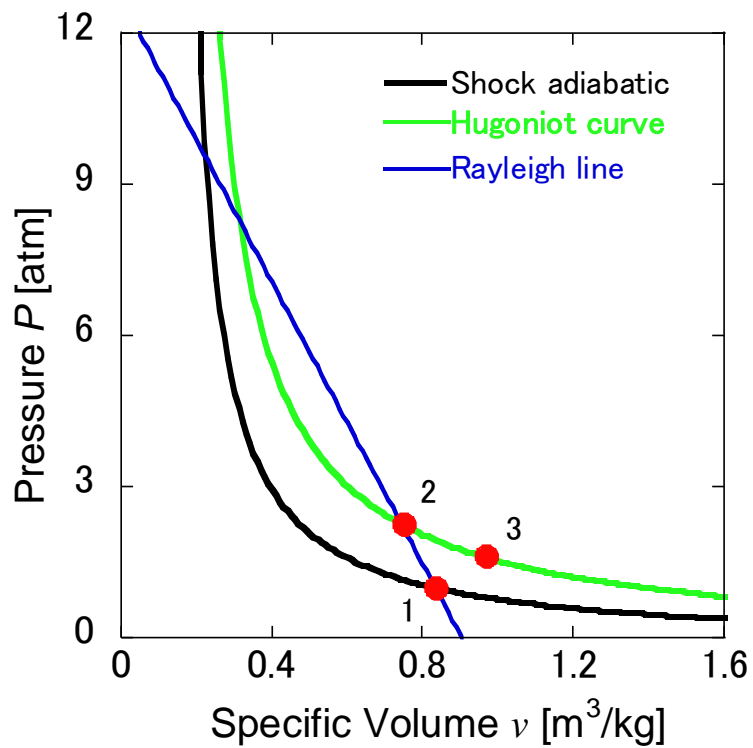


Figure 2-27 p - v diagram for the Overdriven MSD regime

2.9.4 C-J MSD point

The p - v diagram is shown in Figure 2-28. Since there is only one discontinuity, only one Rayleigh line appears. At other microwave power densities, the velocity of

heating region and shockwave are different, thus making two different Rayleigh lines. This is because the control volume for each discontinuity is different caused by the different velocities of the discontinuities.

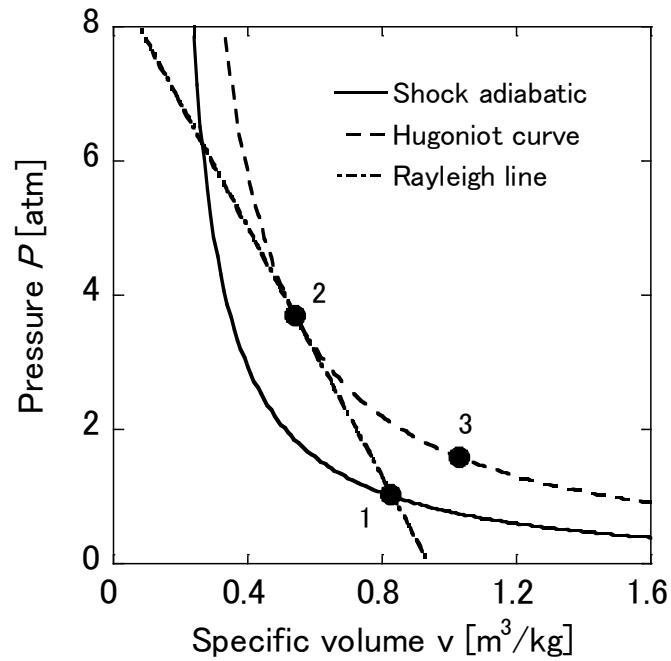


Figure 2-28 p - v diagram for the C-J MSD point

2.10 Boundary between the MSC and MSD regime

Computational results showed that the ionization front and shock wave propagate at the same velocity where the microwave power density is $S_0 \geq 0.196 \text{ MW/cm}^2$, or $S_{\text{average}} \geq 0.022 \text{ MW/cm}^2$. This value could be obtained by comparing the propagating velocity of the ionization front and the C-J velocity. For simplicity, a steadily propagating detonation in a quiescent gas is considered, and a control volume around the detonation wave is set. The governing equations will be as follows:

$$\rho_1 u_1 = \rho_2 u_2 \quad (2-31)$$

$$p_1 + \rho_1 u_1^2 = p_2 + \rho_2 u_2^2 \quad (2-32)$$

$$C_p T_1 + \frac{1}{2} u_1^2 + q = C_p T_2 + \frac{1}{2} u_2^2 \quad (2-33)$$

In the Chapman-Jouget condition, the state 2 in the downstream is thermally choked, or the local propagating velocity is same as the speed of sound.

$$u_2 = a_2 = \sqrt{\gamma R T_2} \quad (2-36)$$

Here a is the speed of sound. By considering that C_p could be written as $C_p = \gamma R / (\gamma - 1)$, the propagating Mach number of the detonation could be written as follows:

$$M_{CJ} = \sqrt{\frac{(\gamma^2 - 1)q}{2a_1^2} + 1} + \sqrt{\frac{(\gamma^2 - 1)q}{2a_1^2}} \quad (2-37)$$

Therefore, the propagating velocity of the detonation in C-J condition could be written as follows:

$$u_1 = D_{CJ} = a_1 \times M_{CJ} = a_1 \left(\sqrt{\frac{(\gamma^2 - 1)q}{2a_1^2} + 1} + \sqrt{\frac{(\gamma^2 - 1)q}{2a_1^2}} \right) \quad (2-38)$$

In the detonation supported by an electromagnetic beam, the heat emission is $q = \eta S_0 / \rho_1 u_1 = \eta S_0 / \rho_1 D_{CJ}$ therefore:

$$D_{CJ} = a_1 \left(\sqrt{\frac{(\gamma^2 - 1)}{2a_1^2} \frac{\eta S_0}{\rho_1 D_{CJ}} + 1} + \sqrt{\frac{(\gamma^2 - 1)}{2a_1^2} \frac{\eta S_0}{\rho_1 D_{CJ}}} \right) \quad (2-39)$$

It is difficult to analytically solve Eq. (2-39), thus the Newton-Rapson method is applied to numerically solve the equation. The result is shown in Figure 2-29, along with the velocity of the microwave discharged ionization front given by Eq. (2-1).

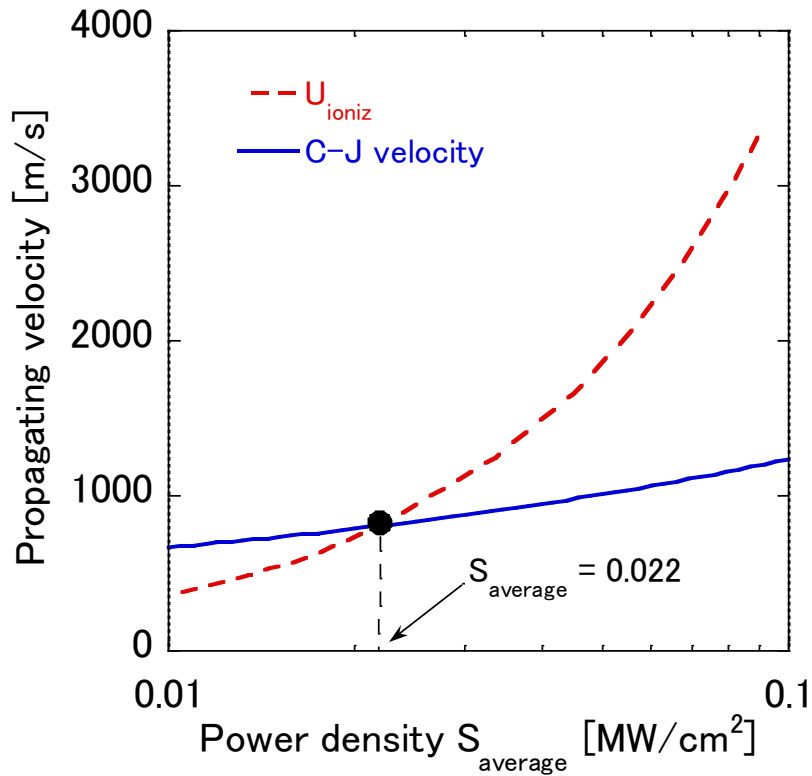


Figure 2-29 Theoretical C-J velocity and measured propagating velocity of ionization front

Figure 2-29 shows that the propagating velocity, increasing with the power density, exceeds the C-J velocity at some point. Since the C-J velocity is the minimum possible velocity of a detonation, the region where $U_{\text{ioniz}} \geq D_{\text{CJ}}$ could be defined as the region of a detonation, in which the power region is $S_{\text{average}} \geq 0.022 \text{ MW/cm}^2$. This result corresponds to the boundary of the C-J MSC regime and the C-J MSD point, which is the boundary of the MSC and the MSD regime.

2.11 A new theory for the Microwave Supported Detonation

As discussed above, a single control volume around the entire flow field could be set in order to analyze the wave structure. Here again, the governing equations are:

$$\rho_i u_i = \rho u \quad (2-40)$$

$$p_i + \rho_i u_i^2 = p + \rho u^2 \quad (2-41)$$

$$C_p T_i + \frac{1}{2} u_i^2 + q = C_p T + \frac{1}{2} u^2 \quad (2-42)$$

For a chemically driven detonation, the structure is known to have a ZND structure, as illustrated in Figure 2-30.

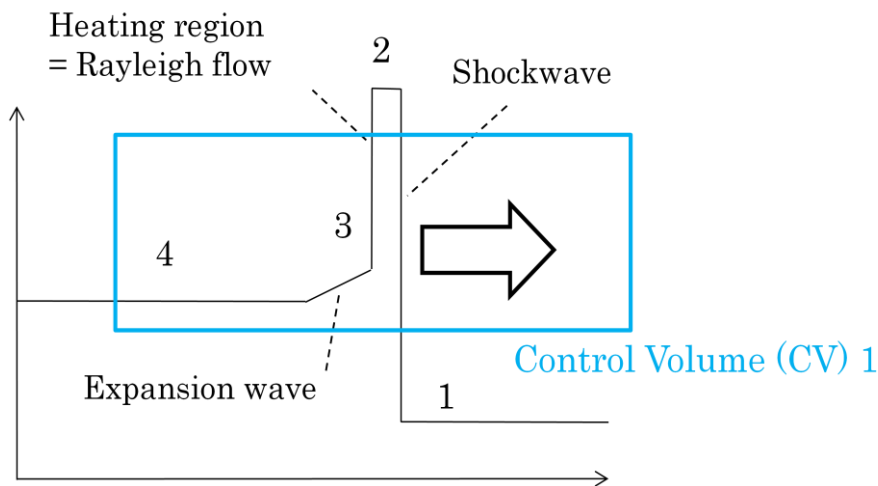


Figure 2-30 Control volume for the ZND detonation model

In Figure 2-30, the shock wave and the heating region, or the combustion zone, are propagating at the same velocity, and we could apply Eqs. (2-31)-(2-33) for the control volume. It is known that there is a delay between the shock wave compression and ignition of the gas, thus there is a distance between the shock wave and the heating region, shown as state 2 in Figure 2-30. The ZND structure could be explained in a p - v diagram using the Rayleigh line, Hugoniot curve and the Shock adiabatic curve.

For a chemical detonation, q is given as a physical property of the premixed gas. If we assume that the propagating velocity is known, we could determine every curve and line in the p - v diagram, as illustrated in Figure 2-31.

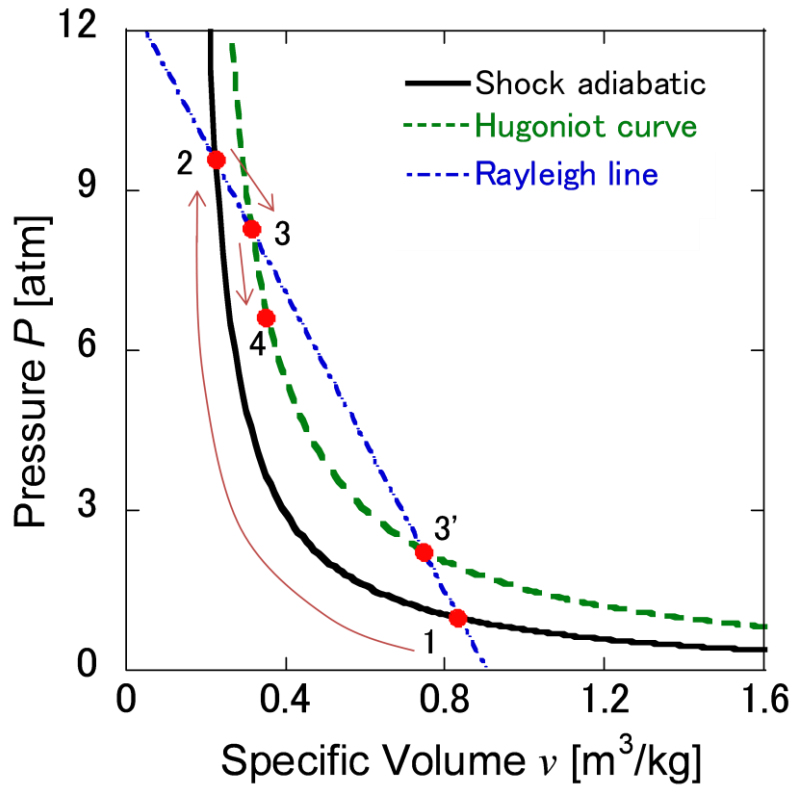


Figure 2-31 p - v diagram for the ZND detonation model

The change at the shock wave, from state 1 to 2, is given along the Shock adiabat curve, where state 2 is determined by the intersecting point of the Shock adiabat curve and the Rayleigh line. Then the change at the reaction zone, from state 2 to 3, is given along the Rayleigh line, where state 3 is determined by the intersecting point of the Rayleigh line and the Hugoniot curve. Although there are two intersecting points between the Rayleigh line and the Hugoniot curve, state 3' is a physically impossible state. This is because the change from state 2 to 3' is a change from a subsonic flow to a

supersonic flow, which is a physically impossible change in the theory of compressible hydrodynamics.

For a detonation supported by an electromagnetic beam, the propagating mechanism is more complex than a chemical detonation. Therefore, if we set a control volume around the detonation wave, the detailed structure is not known, as shown in Figure 2-32. In order to analyze the structure, a p - v diagram written by determining the Rayleigh line, Hugoniot curve and the Shock adiabatic curve is shown in Figure 2-33.

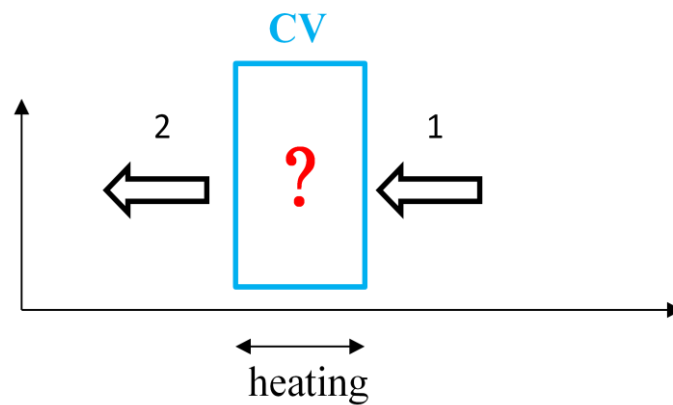


Figure 2-32 Control volume for the microwave supported detonation

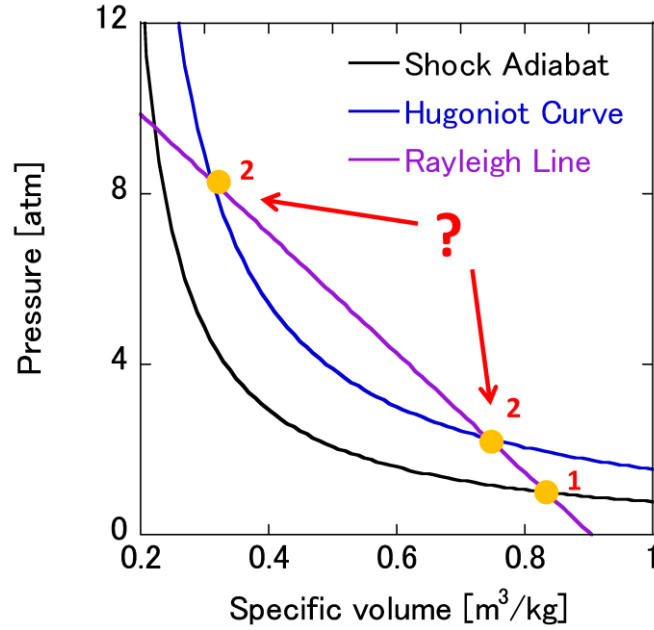


Figure 2-33 p - v diagram for the microwave supported detonation

The state behind the detonation wave should satisfy the governing equations, i.e. the final state should pass through the Rayleigh line and the Hugoniot curve. As mentioned above, there are two possibilities for the final state, and it could not yet be determined. For a chemical detonation, the final state was determined using the p - v diagram based on the knowledge of a ZND structure.

Here, going back to the governing equations, the heat emission could be written as $q = \eta S_0 / \rho_i u_i$, and the energy equation will be written as follows:

$$C_p T_i + \frac{1}{2} u_i^2 + \frac{S_0}{\rho_i u_i} = C_p T + \frac{1}{2} u^2 \quad (2-43)$$

The above relation requires the velocity, u , in order to determine, thus the Hugoniot curve also requires the velocity to be determined. Raizer derived a relation which only requires the power density of the beam, assuming a high compression. [44]

$$p_2 = \left(\frac{2S_0 \rho_1^{1/2} \sqrt{1 - v_2/v_1}}{\eta(\gamma + 1)/(\gamma - 1) - 1} \right)^{2/3} \quad (2-44)$$

Although from the simulated results, the pressure behind the MSD wave is not high enough so that the initial state could be ignored. Thus a similar relation without any further assumptions is derived.

Eliminating variable u from Eqs. (2-31), (2-32) and (2-43), the following equation is obtained.

$$\left(\frac{\gamma+1}{\gamma-1} \frac{v_2}{v_1} - 1\right) \frac{p_2}{p_1} - 2 \frac{1}{p_1 v_1} \sqrt{v_1 - v_2} \frac{1}{\sqrt{p_2 - p_1}} S_0 = \frac{\gamma+1}{\gamma-1} - \frac{v_2}{v_1} \quad (2-45)$$

In order to analytically solve further, a variable substitution is done for the pressure.

$$\sqrt{p_2 - p_1} = x \quad (2-46)$$

Then, Eq. (2-45) is written as follows:

$$x^3 + \frac{2\gamma(v_2 - v_1)}{v_2(\gamma+1) - v_1(\gamma-1)} p_1 x - \frac{2(\gamma-1)\sqrt{v_1 - v_2}}{v_2(\gamma+1) - v_1(\gamma-1)} S_0 = 0 \quad (2-47)$$

For a monic polynomial, $x^3 + ax^2 + bx + c = 0$, the general formula for all three roots are written as follows. [45]

$$x_1 = -\frac{1}{3} \left(a + \sqrt[3]{\frac{m + \sqrt{n}}{2}} + \sqrt[3]{\frac{m - \sqrt{n}}{2}} \right) \quad (2-48)$$

$$x_2 = -\frac{1}{3} \left(a + \omega_2 \sqrt[3]{\frac{m + \sqrt{n}}{2}} + \omega_1 \sqrt[3]{\frac{m - \sqrt{n}}{2}} \right) \quad (2-49)$$

$$x_3 = -\frac{1}{3} \left(a + \omega_1 \sqrt[3]{\frac{m + \sqrt{n}}{2}} + \omega_2 \sqrt[3]{\frac{m - \sqrt{n}}{2}} \right) \quad (2-50)$$

where

$$m = 2a^3 - 9ab + 27c \quad (2-51)$$

$$k = a^2 - 3b \quad (2-52)$$

$$n = m^2 - 4k^3 = (2a^3 - 9ab + 27c)^2 - 4(a^2 - 3b)^3 \quad (2-53)$$

$$\omega_1 = -\frac{1}{2} + \frac{1}{2}\sqrt{3}i \quad (2-54)$$

$$\omega_1 = -\frac{1}{2} - \frac{1}{2}\sqrt{3}i \quad (2-55)$$

The discriminant for the cubic equation is defined as follows:

$$\Delta = 18abc - 4a^3c + a^2b^2 - 4b^3 - 27d^2 \quad (2-56)$$

The discriminant for Eq. (2-47) is $\Delta < 0$ for the region considered in this work, in which the equation has one real root and two non-real complex conjugate roots.

Above all, by considering only the real roots for Eq. (2-47), the pressure behind the MSD wave could be written as follows:

$$p_2 = x^2 + p_1 \quad (2-57)$$

$$x = -\frac{1}{3} \left(\sqrt[3]{\frac{m + \sqrt{n}}{2}} + \sqrt[3]{\frac{m - \sqrt{n}}{2}} \right)$$

$$m = -27 \frac{2(\gamma - 1)\sqrt{v_1 - v_2}}{v_2(\gamma + 1) - v_1(\gamma - 1)}$$

$$n = 729 \left(\frac{2(\gamma - 1)\sqrt{v_1 - v_2}}{v_2(\gamma + 1) - v_1(\gamma - 1)} \right)^2 + 108 \left(\frac{2\gamma(v_2 - v_1)}{v_2(\gamma + 1) - v_1(\gamma - 1)} p \right)^3$$

The relation described in Eq. (2-44) and Eq. (2-57) for $S_0 = 0.240 \text{ MW/cm}^2$, in the Overdriven MSD regime, is shown in Figure 2-24 along with the curves in Figure 2-33. Here, the curve given by Eq. (2-44) is called the Raizer curve, and the curve by Eq. (2-57) the Proposed MSD curve. In Figure 2-33, there were two possible solutions for the pressure behind the MSD wave, but since the solution have to satisfy Eq. (2-57) also, the desired solution should pass the Proposed MSD curve. Thus, as shown in Figure 2-34, the solution behind the MSD wave is with the lower pressure. It is interesting that this point could not be achieved in a chemical detonation, as explained in Chap. 1.6. Additionally, since the Raizer curve does not pass the intersecting point between the Rayleigh line and Hugoniot curve, it would not be appropriate to assume a high compression as done in Eq. (2-44).

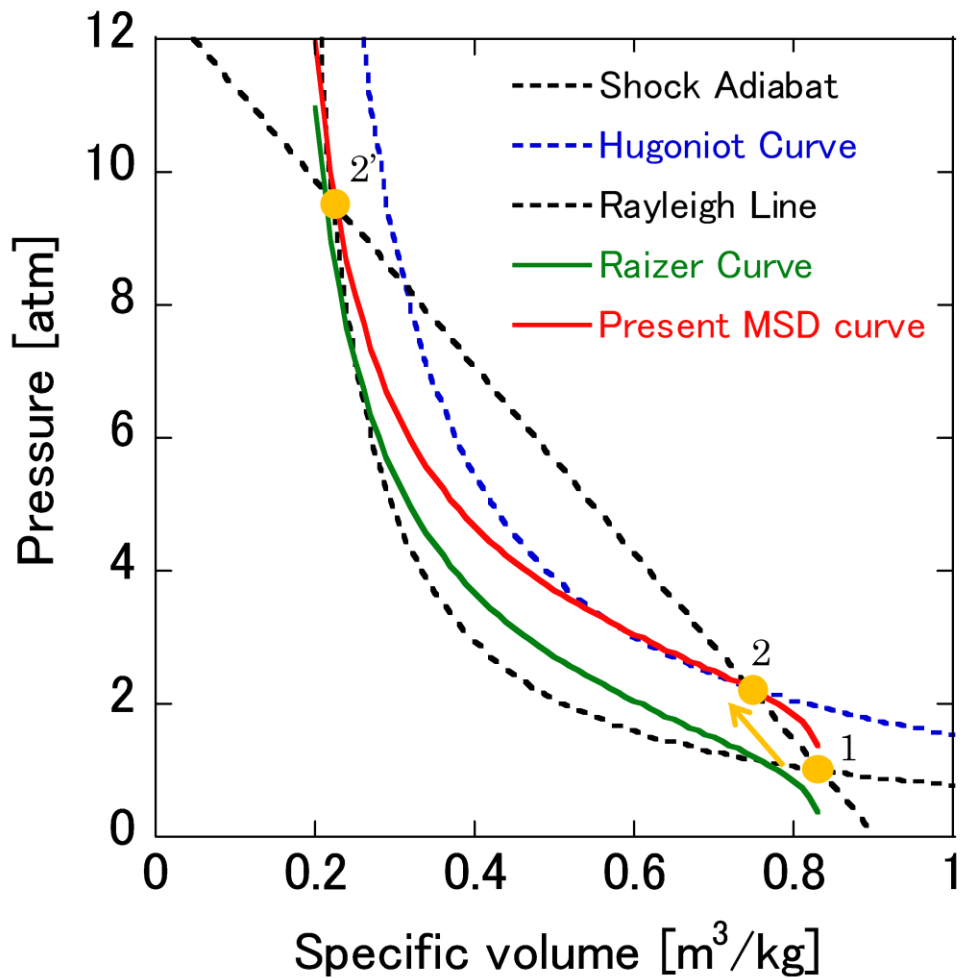


Figure 2-34 p - v diagram for the microwave supported detonation with the proposed MSD curve

By using the results in Figure 2-34, we could determine the structure of the Overdriven MSD wave. If we assume a ZND structure for the Overdriven MSD wave, the change at the shock wave has to change along the Shock adiabetic curve to state 2', which is the von Neumann spike. Since the analysis using the control volume concluded that the final state has to be state 2, the change behind the shock wave has to pass along the Rayleigh line from state 2' to state 2. As explained in Chap. 1.6, this change violates the physics of compressible hydrodynamics, because the flow could only be accelerated to sonic speed. Thus, it could be said that the state at the MSD wave changes from state 1 to 2 along the Rayleigh line, and not passing the Shock adiabetic curve. This result

indicates that the shock wave does not propagate independently, but only within the heating region.

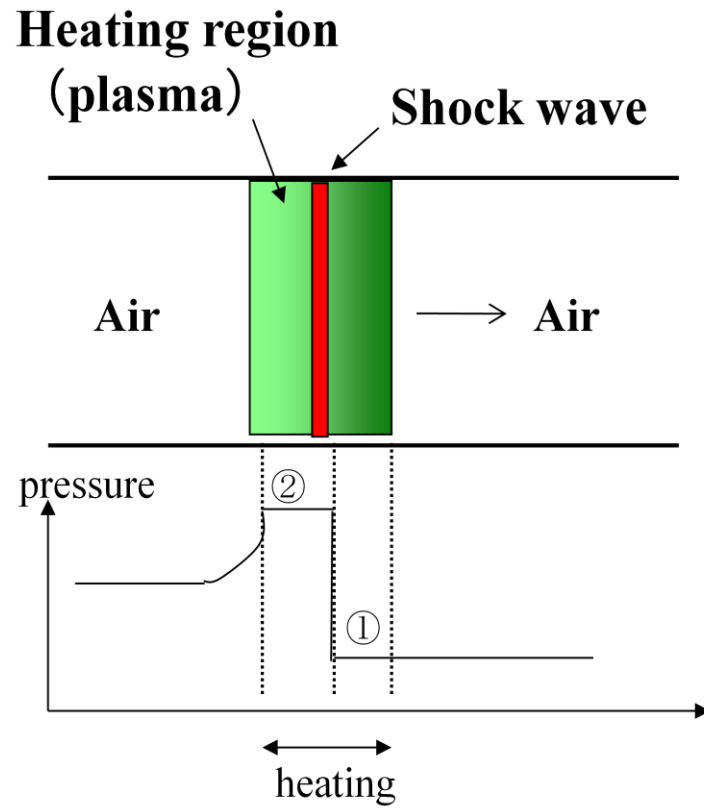


Figure 2-35 Structure of a microwave supported detonation

3. Chemical equilibrium calculation

From the simulated results on the efficiency for the Microwave Rocket, both C_m and heat conversion efficiency was maximum at the C-J MSC regime. By increasing the microwave power, the propagating wave would become a detonation and the efficiencies saturated after some decrease. On the other hand, the energy efficiency for a Laser Supported Detonation (LSD) has been investigated. [39] In order to look further into the energy conversion, in terms of gas dynamics, a chemical equilibrium calculation is conducted.

3.1 Governing equations

The simulated model is shown in Figure 3-1.

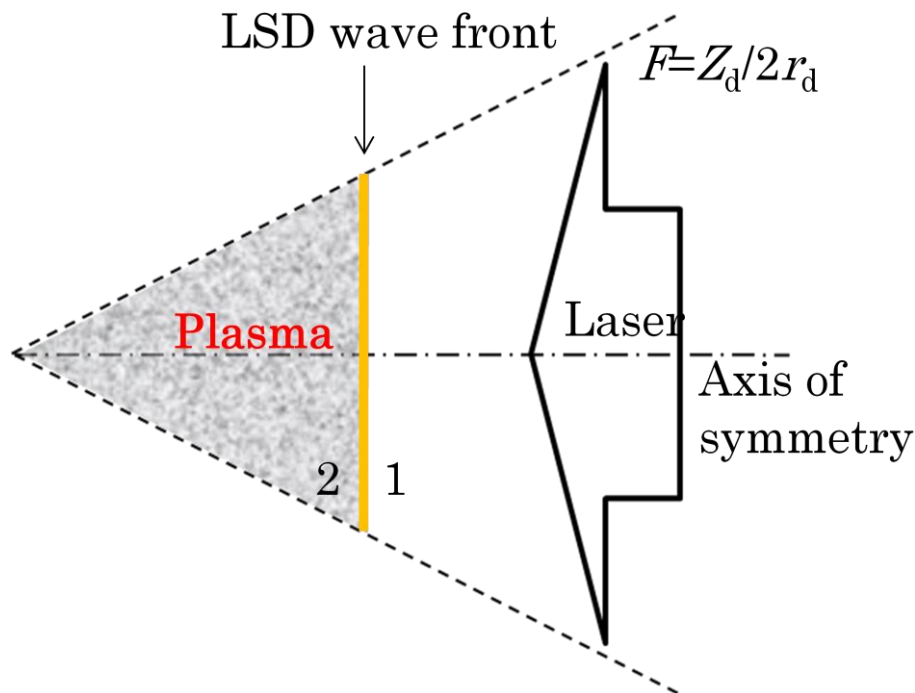


Figure 3-1 Calculation domain for the LSD wave

Here, the LSD wave is assumed planar propagating the pathway of the laser. The physical properties of the upstream and downstream of the LSD wave is assumed

unformed. The physical values are calculated by a chemical equilibrium computation and by solving the LSD relations.[47][48] The governing equations are as follows:

$$h_2 = \frac{1}{2}\gamma_2 R_2 T_2 = h_1 + \frac{1}{2}D_{CJ}^2 + \frac{P_L/A_L}{\rho_1 D_{CJ}} \quad (3-1)$$

$$v_2^2 = \frac{\gamma_2 p_2}{\rho_2} = \frac{\gamma_2^2}{(\gamma_2 + 1)^2} \left(\frac{p_1 + \rho_1 D_{CJ}^2}{\rho_1 D_{CJ}} \right)^2 \quad (3-2)$$

$$\rho_2 = \frac{(\gamma_2 + 1)\rho_1 D_{CJ}^2}{\gamma_2 (p_1 + \rho_1 D_{CJ}^2)} \quad (3-3)$$

$$\sum_{s=1}^{n_{sp}} \nu_{r,s} \tilde{X}_s - \ln K_{eq}^r = 0 \quad (3-4)$$

$$\sum_{s=1}^{n_{sp}} \xi_s^c \exp(\tilde{X}_s) - Y_0^c \rho_2 = 0 \quad (3-5)$$

Eq. (3-1) is the energy equation, where subscript 1 indicates the surrounding atmosphere and subscript 2 the properties behind the LSD wave. The velocity is based on a LSD fixed coordinates, and the inflow is given from experimental results. Here, the LSD wave is assumed to satisfy the Chapman-Jouget condition, thus the velocity behind the LSD wave could be described as follows:

$$v_2 = \sqrt{\gamma_2 R_2 T_2} \quad (3-6)$$

P_L and A_L indicate the laser power and the cross-section of the LSD wave. Eqs. (3-2) and (3-3) indicate the Hugoniot relation assuming the C-J condition.

Eq. (3-4) is the equation for the detailed chemical equilibrium, where n_{sp} , $\nu_{r,s}$ and K_{eq}^r are the number of species, the stoichiometric coefficient and the chemical equilibrium constant, respectively. \tilde{X}_s is defined as $\tilde{X}_s = \ln X_s$, where X_s is the number of moles per unit volume. Eq. (3-5) is the mass conservation law for the basic element c . For air, $c=N, O, e^-$. Furthermore, ξ_s^c is the number of basic elements in chemical specie s , and Y

c_0 is the number of moles per unit volume of the basic element, which is given as a constant.

For a line focused system, A_L is given from the F number as follows:

$$F = \frac{z_d}{2r_d} \quad (3-7)$$

$$A_L = l \frac{z_d}{F} \quad (3-8)$$

Here, z_d is the position of the LSD front, and l is the distance between the two plates.

The position of the LSD wave is calculated as follows:

$$\frac{dz_d}{dt} = v_1 \quad (3-9)$$

By calculating the propagation of the LSD wave, the blast wave conversion efficiency E_B is calculated using the following equation.

$$\dot{m} = \rho_1 v_1 A_L \quad (3-10)$$

$$E_B = \int \dot{m} (h_2^{t+r+k} - h_1^{t+r+k}) dt \quad (3-11)$$

Here, h^{t+r+k} is the sum of translational, rotational and kinetic energy.

In order to calculate the physical properties, Eqs. (3-1)-(3-5) are solved with $\ln T_2$, ρ_2 and \tilde{X}_s as an unknown variable. The modified Newton-Rapson method by Botton et al. is used.[49]

3.2 Thermodynamic properties

The internal energy of a gas consists of the formation energy Δe^f and four energy modes: the translational energy e_{trans} due to thermo motion, rotational energy e_{rot} for molecules, vibrational energy e_{vib} of molecules and electron excitation energy e_{ex} .

$$e_{molecule} = e_{trans} + e_{rot} + e_{vib} + e_{ex} + \Delta e^f \quad (3-12)$$

$$e_{atom} = e_{trans} + e_{ex} + \Delta e^f \quad (3-13)$$

$$e_{electron} = e_{trans} \quad (3-14)$$

For each of the four energy modes, there exists a specific temperature, namely the translational temperature, rotational temperature, vibrational temperature and the electron excitation temperature. When all of these temperatures are different, the gas is in thermodynamic non-equilibrium.[50]

In the LSD wave, electrons absorb energy of the laser beam through inverse bremsstrahlung and distribute the energy to the heavy particles by collisions.[49] Thus in the LSD wave, there is a possibility that the electron translational temperature is in non-equilibrium with other temperatures. Although, it could be considered that the collision frequency is high because a high-density and high-temperature plasma generated by the strong shock wave. Thus a fast relaxation between different temperature modes could be assumed, and a one-temperature model is applied in this study.

In the one-temperature model, the internal energy and enthalpy of chemical species could be defined as follows:

$$e_s = \int_{T_{ref}}^T C_{v,s}(T)dT + \Delta e_s^f \quad (3-15)$$

$$h_s = \int_{T_{ref}}^T C_{p,s}(T)dT + \Delta h_s^f \quad (3-16)$$

Here, $C_{p,s}=C_{v,s}+R_s$, and when $T_{ref}=0$, $\Delta h_s^f=\Delta e_s^f$. Further in this study, the reference temperature $T_{ref}=0$.

The specific heat at constant pressure, C_p , could be written as a sum for each energy mode.

$$C_{p,s} = C_{p,trans,s} + C_{p,rot,s} + C_{p,vib,s} + C_{p,ex,s} \quad (3-17)$$

Generally, the vibrational and electron excitation mode of a gas are not excited at standard temperature.

$$C_{p,vib,s} = C_{p,ex,s} = 0 \quad (3-18)$$

On the other hand, the translational and rotational energy modes are excited, which could be described as follows:

$$C_{p,trans,s} = \frac{5}{2}R_s, \quad C_{p,rot,s} = 2R_s \quad (3-19)$$

Therefore, h^{t+r+k} in Eq. (3-11) could be written as follows:

$$h^{t+r+k} = \sum_s^{n_{sp}} \frac{\rho_s}{\rho} (C_{p,trans,s} + C_{p,rot,s}) T + \frac{1}{2} u^2 \quad (3-20)$$

When the temperature increases, the vibrational and electron excitation energy mode will excite, and the temperature dependence of $C_{p,s}$ should be considered. In this research, the temperature polynomial by Gupta is applied for $T < 30,000\text{K}$. [51]

$$C_{p,s} = R_s \sum_{k=1}^5 A_k^s T^{k-1} \quad (3-21)$$

For temperature higher than 30,000K, the temperature polynomial by Balakrishnan is applied. [52]

$$C_{p,s} = a_s + b_s T + \frac{c_s}{T^2} \quad (3-22)$$

3.3 Chemical equilibrium calculation

Chemical equilibrium state is achieved when the characteristic time of the chemical reaction is fast enough than the characteristic time of the flow field. [50] As described above, it could be said that the collision frequency is high in the LSD wave, thus the reacting speed is very fast. Therefore, here a chemical equilibrium is assumed.

The number of detailed equilibrium equations described in Eq. (3-4) should be $n_{sp} - n_c$, in order to calculate. Here, a molecular ion will not be important for the equilibrium calculation. Therefore, the species considered for air are N_2 , O_2 , NO , N^+ , O^+ , N , O and e^- . ξ_s^c , the number of basic element c in specie s , required in Eq. (3-5) is given in Table 3-2. Y_0^c is defined as follows:

$$Y_0^c = \sum_s^{n_{sp}} \frac{\xi_s^c X_{s1}}{\rho_1} \quad (3-23)$$

Here, X_{s1} is the number of moles per unit volume before the laser heating, which is $X_{N21}:X_{O21}=4:1$ for air.

For the chemical equilibrium constant, K_{eq}^r , the temperature polynomial by Gupta is applied.⁵⁾

$$\ln K_{eq}^r = A_{K_{eq}}^r Z^5 + B_{K_{eq}}^r Z^4 + C_{K_{eq}}^r Z^3 + D_{K_{eq}}^r Z^2 + E_{K_{eq}}^r Z + F_{K_{eq}}^r \quad (3-24)$$

$$Z = \ln \frac{10^4}{T} \quad (3-25)$$

Table 3-1 Chemical reactions for eight species used for equilibrium calculation

Elements: N ₂ , O ₂ , NO, N ⁺ , O ⁺ , N, O, e ⁻	
Basic Elements: N, O, e ⁻	
No.	Reaction
1	N ₂ ↔ 2N
2	O ₂ ↔ 2O
3	NO ↔ N+O
4	N ↔ N ⁺ +e ⁻
5	O ↔ O ⁺ +e ⁻

Table 3-2 Number of basic elements for the eight species for air

Species	ξ^N	ξ^O	ξ^{e^-}
N ₂	2	0	0
O ₂	0	2	0
NO	1	1	0
N ⁺	1	0	-1
O ⁺	0	1	-1
N	1	0	0
O	0	1	0
e ⁻	0	0	1

3.4 Verification

The code was verified by calculating the mole fraction of chemical species of air at various temperatures. Results are shown in Figure 3-2 along with the results by Vincenti. Calculated result show good agreement with literature-based results, and the chemical equilibrium calculation is verified.

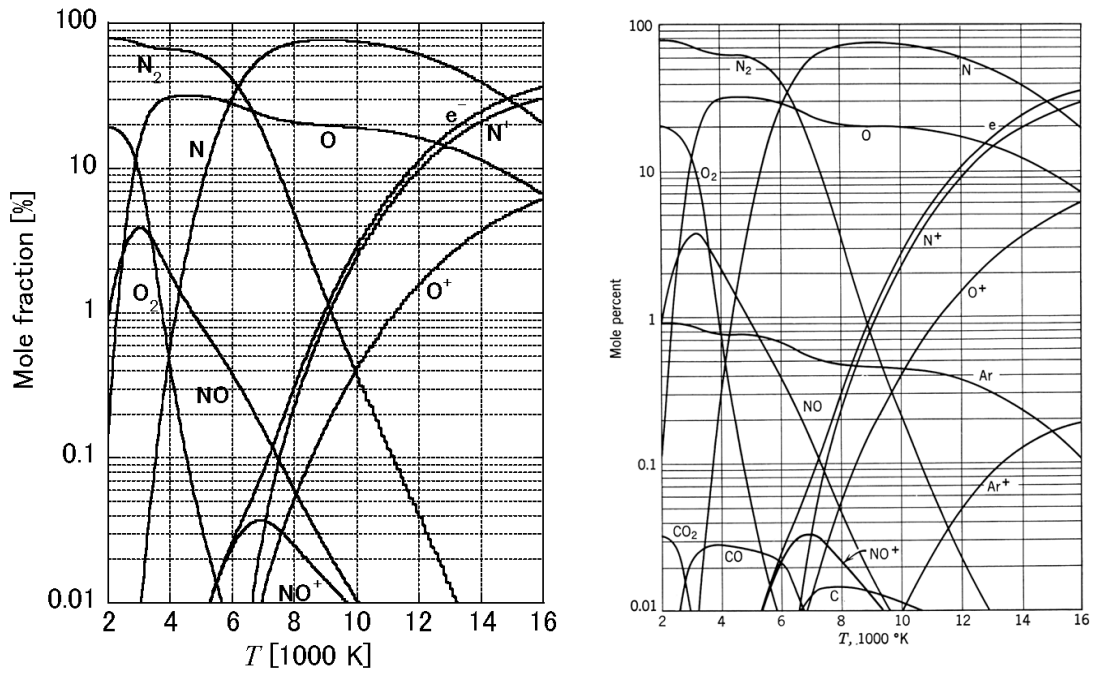


Figure 3-2 Comparison of mole fraction at each temperature

3.5 Calculation of the LSD wave

In order to simulate the three-dimensional LSD wave, the propagating history and laser power are given from measured results. The propagating history of the ionization front and shock wave are shown in Figure 3-3.

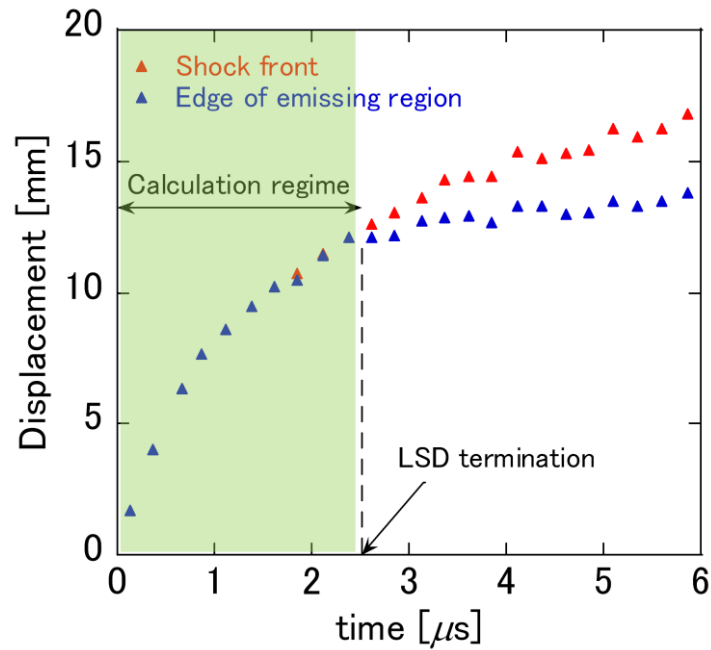


Figure 3-3 Measured propagating history of ionization front and shock front

In Figure 3-3, the ionization front and shock wave separate at around $t=2.5\mu\text{s}$, thus the calculation will be considering from ignition until $t=2.5\mu\text{s}$.

The measured laser power history and the propagating velocity are shown in Figure 3-4. The propagating velocity is given by differentiating the curve fitted function in Figure 3-3. By assuming a complete absorption in the plasma, the physical state behind the LSD is simulated.

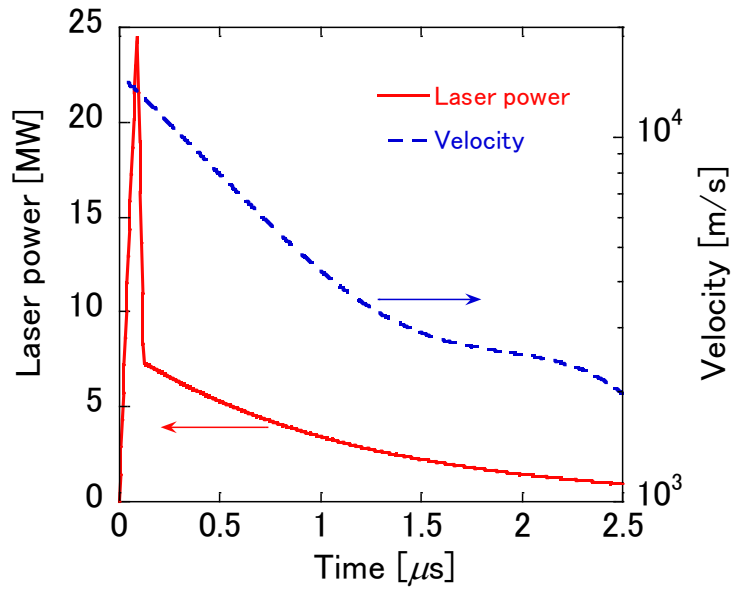


Figure 3-4 Measured laser power history and propagating velocity of ionization front

3.6 Results and discussions

The calculated temperature behind the LSD wave, along with the laser power history, is shown in Figure 3-5. At $t=0$, when ignition happens by the sharp increase of laser power, the temperature of the plasma is about 90,000K. When the laser power suddenly decreases at $t=0.2\mu\text{s}$, the plasma temperature suddenly decreases at the same time. Since a thermodynamic equilibrium is assumed in this calculation, the laser power supplied to the electrons is exchanged with heavy particles, and thus the plasma temperature shows similar tendencies with the laser power.

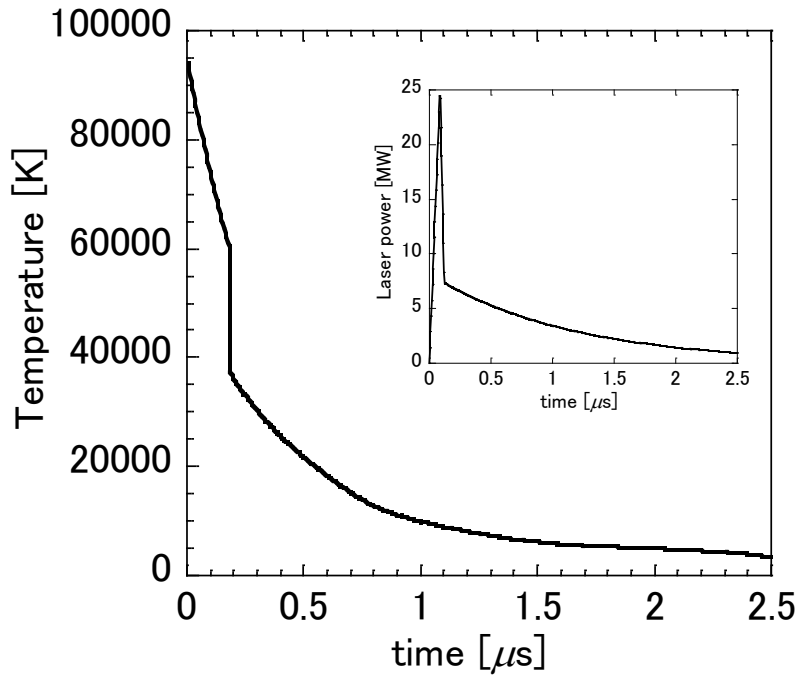


Figure 3-5 Calculated temperature behind the LSD front

The history of mole fraction for each chemical species are shown in Figure 3-6. From ignition to $t=0.4\mu s$, the plasma is completely ionized. At $t=0.4\mu s$, neutral particles are discontinuously increasing. On the other hand, the discontinuous change in temperature happens at around $t=0.2\mu s$. Therefore, the discontinuous change in mole fraction of species is not due to the change in temperature. From Figure 3-5, the temperature range the current chemical model is considering is much less than the simulated temperature soon after ignition. Thus, this result implies that there should be a multiple charged ion considered in the current phenomena.

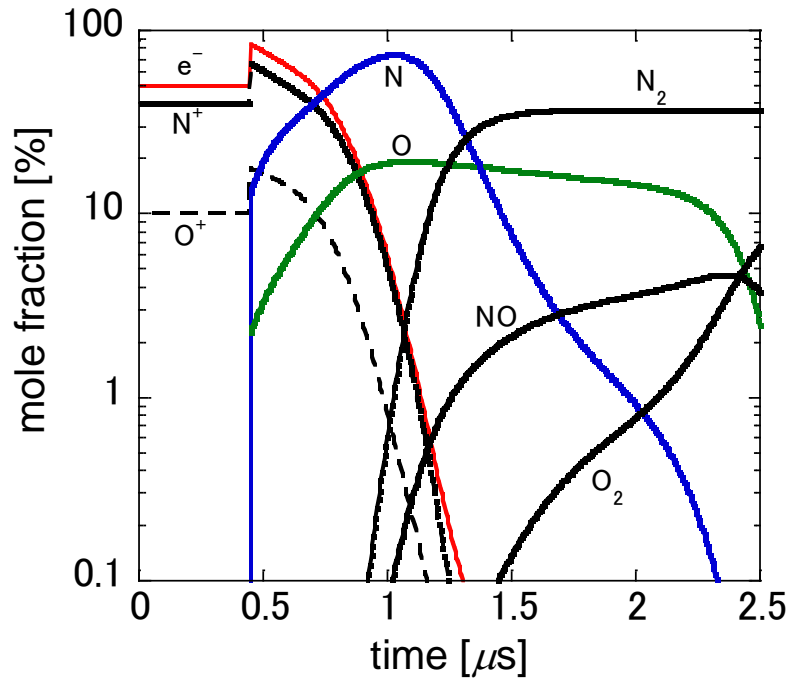


Figure 3-6 Calculated mole fraction behind the LSD front

The condition of the LSD termination has been investigated experimentally in terms of electron density and laser power density. The electron density and temperature are shown in Figure 3-7, and the irradiated laser power density on the LSD wave is shown in Figure 3-8. Note that since a one-temperature model is applied here, the electron temperature is equal to other temperatures. Table 3-2 shows the experimental conditions for the LSD termination, which is also illustrated in Figure 3-7. At $t=2.5\mu\text{s}$, which is when the LSD terminates, both the electron density and temperature are underestimated compared with experimental results. From experiments done by Fukui, the electron temperature is kept over 10,000K during the LSD process.[54] Additionally, the electron density required to keep the LSD propagation should be kept at around 4.95×10^{24} . [53] These underestimations are a result of assuming thermal and chemical equilibrium, thus for further comparison with experimental results, a numerical analysis based on thermal and chemical non-equilibrium is required.

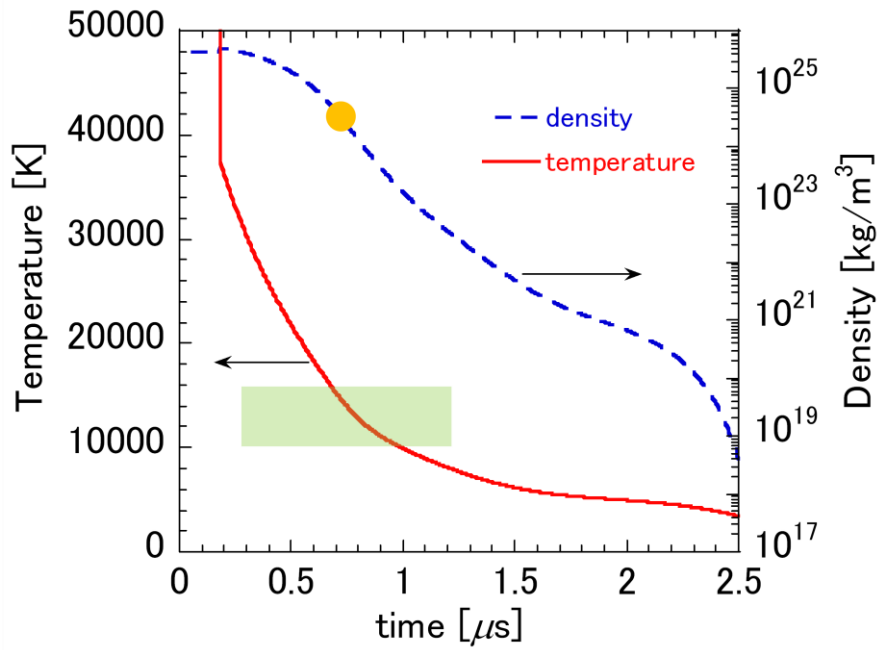


Figure 3-7 Calculated electron density and temperature behind the LSD front

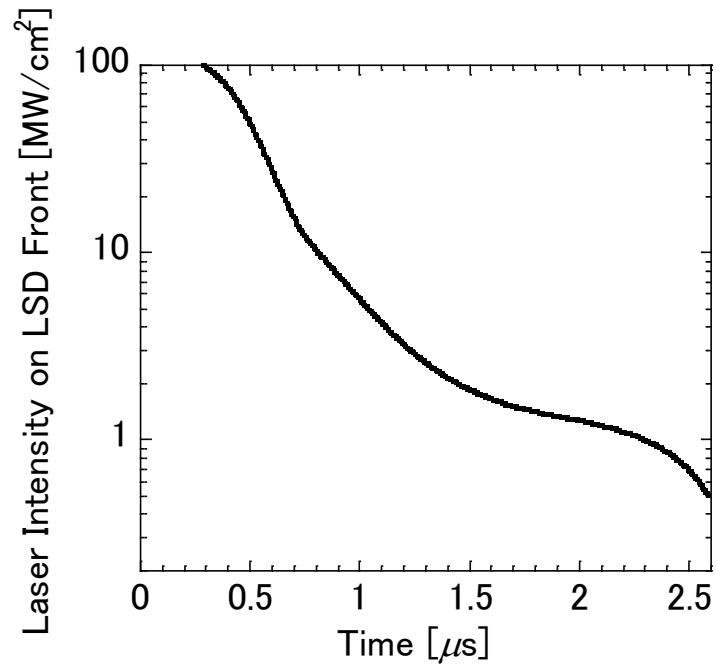


Figure 3-8 Irradiated laser power density on LSD front

	LSD	Post LSD
Electron density	2×10^{24}	$1 \sim 1.5 \times 10^{24}$
Heating rate [MW/m ³]	$10 \sim 15 \times 10^7$	$5 \sim 6 \times 10^7$
Absorption layer [mm]	0.3	0.5

4. Conclusions

1. The microwave driven shock waves in the Microwave Rocket was numerically investigated. By changing the microwave power density, the flow field was categorized into three regimes and one point, namely the MSC regime, C-J MSC regime, Overdriven MSD regime and the C-J MSD point.
2. Theoretical analysis for the Overdriven MSD regime showed that the propagating shock wave could only exist in a heating region, and does not propagate independently. This structure is different from the ZND structure, which is a theoretical structure for a chemical detonation. Furthermore, a new formula to calculate the pressure behind the microwave detonation was deduced.
3. By assuming thermo-chemical equilibrium for the LSD, a discontinuous change in the chemical species was observed, which implied the existence of multi-ionized species. Furthermore, calculated density and temperature for electrons were underestimated compared with experimental results. This implied that a strong non-equilibrium exists during the generation and propagation of the LSD wave in atmospheric air.

Bibliography

- [1] *Space Factory on International Space Station*, ed by Ebisuzaki, T., Handa, T., and Takahashi, Y., Universal Academy Press, Tokyo, Japan, 2000.
- [2] Glaser, P., "Power from the Sun: Its Future," *Science Magazine*, Vol 162, 1968, pp 857-861.
- [3] Nishioka, K., Arno, R. D., Alexander, A. D., and Slye, R. E., "Feasibility of Mining Lunar Resources for Earth Use: Circa 2000 A.D., vols. I, II," vol. I, NASA TM X-62, 267; vol. 2, NASA TM X-62, 268, 1973.
- [4] Sutton, G. P. and Boblarz, O., *Rocket Propulsion Elements*, 7th ed., Wiley-Interscience, New York, 2000.
- [5] *Reducing Space Mission Cost*, ed. by Wertz, J., and Larson, W., Kluwer Academic Publishers, Boston, 1996.
- [6] Hertzberg, A., Bruckner, A. P., and Bogdanoff, D. W., "Ram Accelerator: A new Chemical Method for Accelerating Projectiles to Ultrahigh Velocities," *AIAA Journal*, Vol. 26, 1998, pp. 195-203.
- [7] Hamate, Y., Sasoh, A., and Takayama, K., "High Ram Acceleration Using Open-Base Projectile," *Journal of Propulsion and Power*, Vol. 19, 2003, pp. 190-195.
- [8] Zana, L. M., "Rail Accelerator for Space Transportation," NASA Technical paper, 2571, 1986.
- [9] Fickse, D. A., and Thio, Y. C., "The ELF-I AUGMENTED ELECTROMAGNETIC LAUNCHER," *IEEE TRANSACTIONS ON MAGNETICS*, Vol. 20, 1984.
- [10] Kantrowitz. Propulsion to orbit by ground-based lasers. *Astronautics and Aeronautics*, 10(5):74-76, May 1972.
- [11] Hettche, L. R., Schriempf, J. T., and Stegman, R. L., "Impulse reaction resulting from the in-air irradiation of aluminum by a pulsed CO₂ laser," *Journal of Applied Physics*, Vol. 44, 1973, pp. 4079-4085.
- [12] Pirri, A. N., Schler, R., and Northam, D., "Momentum transfer and plasma formation above a surface with a high-power CO₂ laser," *Applied Physics Letters*, Vol. 21, 1972, pp. 79-81.
- [13] Simons, G. A., "Momentum Transfer to a Surface When Irradiated by a High-Power Laser," *AIAA Journal*, Vol. 22, 1984, pp. 1275-1280.
- [14] Simons, G. A., and Pirri, A. N. "The Fluid Mechanics of Pulsed Laser Propulsion," *AIAA Journal*, Vol.15, 1977, pp. 835-842.
- [15] Pirri, A. N., and Monsler, M. J., "Propulsion by Absorption of Laser Radiation," *AIAA Journal*, Vol. 12, 1974, pp. 1254-1261.
- [16] Ageev, V. P., Barchukov, A. I., Bunkin, F. V., Konov, V. I., Korobeinikov, V. P., Putjatin, B. V., and Hudjakov, V. M., "Experimental and theoretical modeling of laser propulsion," *Acta Astronautica*, Vol. 7, 1980, pp. 79-90.

- [17] Bohn, W. L. "Laser Lightcraft Performance," Proceedings of SPIE, Vol. 3885, 2000, pp. 48-53.
- [18] Myrabo, L. M., Messitt, D. G., and Mead, Jr., F. B., "Ground and Flight Tests of Laser Propelled Vehicle," AIAA Paper 98-1001, 1998
- [19] Sasoh, A., "Laser-Propelled Ram Accelerator," *Journal of Physics IV France*, Vol.10, 2000, pp.41-47.
- [20] J.T.Kare. Laser powered heat exchange rocket for ground-to-orbit launch. *Journal of Propulsion and Power*, 11(3):535{543, 1995.
- [21] J.P. Knecht and M.M. Micci. Analysis of a microwave-heated planar propagating hydrogen plasma. *AIAA Journal*, 26(2):188{194, 1988.
- [22] P. Balaam and M.M. Micci. Investigation of free-oation resonant cavity microwave plasmas for propulsion. *Journal of Propulsion and Power*, 8(1):103{109, 1992.
- [23] G. M. Batanov, S. I. Gritsinin, I. A. Kossyy, A. N. Magunov, V. P. Silakov, and N. M. Tarasova. High pressure microwave discharge. In L.M.Kovrizhnykh, editor, *Plasma Physics and Plasma Electronics*, pages 241{282. Nova Science Publishers Commack, 1989.
- [24] K.L.G. Parkin and F.E.C. Culick. Feasibility and performance of the microwave thermal rocket launcher. In Kimiya Komurasaki, editor, *Beamed Energy Propulsion: Second International Symposium on Beamed Energy Propulsion*, pages 407{417. American Institute of Physics, 2003.
- [25] K.L.G. Parkin, L.D.DiDomenico, and F.E.C. Culick. The microwave thermal thruster concept. In Kimiya Komurasaki, editor, *Beamed Energy Propulsion: Second International Symposium on Beamed Energy Propulsion*, pages 418{429. American Institute of Physics, 2003.
- [26] A.R. Bruccoleri, K.L.G. Parkin, and M. Barmartz. Axial temperature behavior of a heat exchanger tube for microwave thermal rockets. *Journal of Propulsion and Power*, 23(4):889{894, 2007.
- [27] H. Katsurayama, K. Komurasaki, A. Momozawa, and Y. Arakawa. Numerical and engine cycle analyses of a pulse laser ramjet vehicle. *Transactions of JSASS, Space Technology Japan*, 1:9{16, 2003.
- [28] H. Katsurayama, M. Ushio, K. Komurasaki, and Y. Arakawa. Analytical study on ight performance of an air-breathing RP laser launcher. AIAA Paper No. 2004-3585, 40th AIAA/ASME/SAE/ASEE Joint Propulsion Conference and Exhibit, 2004.
- [29] H. Katsurayama, K. Komurasaki, and Y. Arakawa. Feasibility for the orbital launch by pulse laser propulsion. *Journal of Space Technology and Science*, 20(2):32{42, 2005.
- [30] K. Matsuo, "Compressible Fluid Dynamics: Theory and Analysis in Internal Flow", Rikogakusha Publishing Co., Ltd, 2006 (in Japanese)
- [31] Mallard, E. and Le Chatelier, H., *Recherches Experimentales et Theoriques sur la Combustion des Melanges Gaseux Explosifs*, *Ann. Mines*, 8, 4, (1883), pp.274-568.

- [32] Berthelot, M. and Vieille, P., Sur la Vitesse de Propagation des Phenomenes Explosifs dans les Gaz, C. R. Acad. Sci., Paris, 94, (1882), pp. 101-108; (1882), pp. 822-823; 95, (1882), pp. 151-157.
- [33] Hugoniot, H., Propagation du Mouvement dans les Corps, J. Ec. Polyt. Paris, 57e cahier, (1887-1889), pp. 1-125.
- [34] Chapman, D. L., On the Rate of Explosion in Gases, Phil. Mag. 47, Ser. 5, No. 284, (1899), pp. 90-104.
- [35] Crussard, L., Ondes de Choc et Onde Explosive, Bull. Soc. Industr. Min. St-Etienne, 6, Ser. 4, (1907), pp. 257-364.
- [36] Jouguet, E., Mecanique des Explosifs, Encyclopedie Scientifique, Doin et Fils, Paris, (1917).
- [37] Zel'dovich, Y. B., On the Theory of the Propagation of Detonation in Gaseous Systems, Zh. Eksp. Teoret. Fiz. 10, (1940), pp.542-568.
- [38] von Neumann, J., Progress Report on Theory of Detonation Waves, Office of Scientific Research and Development Report No. 549, (1942).
- [39] K. Mori and K. Komurasaki, "Energy transfer from a laser pulse to a blast wave in reduced-pressure air atmospheres", Journal of Applied Physics, Vol. 95, No. 11, June 2004
- [40] T. J. Chung, "Computational Fluid Dynamics", Cambridge University Press 2002
- [41] E. Shima, T. Jounouchi, "Role of Computational Fluid Dynamics in Aeronautical Engineering (No.12), Formulation and Verification of Uni-Particle Upwind Schemes for the Euler Equations," *Proceedings of the 12th NAL Symposium on Aircraft Computational Aerodynamics*, Japan, 1995, pp.255-260.
- [42] Bussing T., and Pappas G., "An Introduction to Pulse Detonation Engines", AIAA 94-0263 (1994)
- [43] Endo T., Kasahara J., Matsuo A., Inaba K., Sato S., and Fujiwara T., "Pressure History at the Thrust Wall of Simplified Pulse Detonation Engine", AIAA Journal, Vol. 42, No. 9, 2004, pp. 1921-1930
- [44] Ya. B. Zel'dovich and Yu. P. Raizer, "Physics of Shock Waves and High-Temperature Hydrodynamic Phenomena", Dover Publications, Inc. Mineola, New York 1966
- [45] Lucye Guilbeau (1930). "The History of the Solution of the Cubic Equation", *Mathematics News Letter* 5 (4), p. 8-12.
- [46] Doering, W. and Burkhardt, Contributions to the Theory of Detonation, VDI Forschungsbericht No. 1939, (1944).
- [47] Raizer, Y.P.: Laser-Induced Discharge Phenomena, Consultants Bureau, New York and London, 1977, Ch.6.
- [48] Landau, L.D. and Lifshitz, E.M.: Fluid Mechanics, 2nd ed., Butterworth-Heinemann, Oxford, 1987, Ch.14.
- [49] Botton, B., Abele, D.V., Carbonaro, M. and Degrez G.: Thermodynamic and Transport

- Properties for Inductive Plasma Modeling, *Journal of Thermophysics and Heat Transfer*, **13**, (1999), pp.343-350.
- [50] Vincenti G.W. and Kruger, C.H.: Introduction to Physical Gas Dynamics, John Wiley and Sons, New York, 1965.
- [51] Gupta, R.N., Yos, J.M., Thompson R.A. and Lee, K.P.: A Review of Reaction Rates and Thermodynamic and Transport Properties for an 11-Species Air Model for Chemical and Thermal Nonequilibrium Calculations to 30,000 K, NASA RP1232, 1990.
- [52] Balakrishnan, A.: Correlations for Specific Heats of Air Species to 50,000 K, AIAA Paper 86-1277, 1986.
- [53] Fukuda, A., et al., "Electron Density Measurement of Laser Supported Detonation Waves," AIAA-2004-3585
- [54] Fukui, A., et al., "LSD Termination Conditions and Post-Shock Electron Density", AIAA-2007-1189

ACKNOWLEDGEMENTS

I would like to express my sincerest appreciation to Professor Kimiya Komurasaki for having me challenge towards this research, and for the research environment. He gave me many opportunities to attend conferences, which gave me the chance to meet and discuss with many people. As a graduate student, his instructions made me think and look back what research should be done; the location of where I am, the roadmap I should make and the vision I should have as a researcher. This thesis could never be completed without his generous instructions.

I would also like to express my sincere thanks to Professor Yoshihiro Arakawa, who told me how an engineer and a researcher should be.

I received many helps from Dr. Makoto Matsui in Shizuoka University, Dr. Yasuhisa Oda in the Japan Atomic Energy Agency and Dr. Shigeru Yokota in the University of Tokyo. Dr. Matsuo gave me direct instructions which helped me make decisions towards my research. Dr. Oda and the Japan Atomic Energy Agency gave me the opportunity to conduct experiments, and held many opportunities to discuss my research.

I would like to express my thanks to Mr. Wang Bin, Mr. Yuya Shiraishi, Mr. Keigo Hatai, Mr. Akifumi Asahara, Mr. Kohei Shimamura and Mr. Yoshihiro Mizuno. As a member of the research group on beamed energy propulsion, the many opportunities discussing work helped me do research.

I would like to express my thanks to all of the members in Arakawa-Komurasaki laboratory, especially, Mr. Takashi Komrau, Mr. Ryo Kondo, Mr. Shinatora Cho, Mr. Satoshi Nomura, Mr. Kentaro Hara, Mr. Suisei Yamagishi and Mr. Toshikazu Yamaguchi. As members in the same grade, we shared joys and sorrows to each other, and I would not have been able to finish my work without you.

Finally, I would like to thank my family for having me study two years in the University of Tokyo.